University of Central Lancashire
UCLan

Central Lancashire Online Knowledge (CLoK)

Title	AGN STORM 2. X. The Origin of the Interband Continuum Delays in Mrk 817 *
Type	Article
URL	https://clok.uclan.ac.uk/53694/
DOI	https://doi.org/10.3847/1538-4357/ad8160
Date	2024
Citation	Netzer, Hagai, Goad, Michael R., Barth, Aaron J., Cackett, Edward M., Horne, Keith, Hu, Chen, Kara, Erin, Korista, Kirk T., Kriss, Gerard A. et al (2024) AGN STORM 2. X. The Origin of the Interband Continuum Delays in Mrk 817 *. The Astrophysical Journal, 976 (1). ISSN 0004-637X
Creators	Netzer, Hagai, Goad, Michael R., Barth, Aaron J., Cackett, Edward M., Horne, Keith, Hu, Chen, Kara, Erin, Korista, Kirk T., Kriss, Gerard A., Lewin, Collin, Montano, John, Arav, Nahum, Behar, Ehud, Brotherton, Michael S., Chelouche, Doron, De Rosa, Gisella, Dalla Bontà, Elena, Dehghanian, Maryam, Ferland, Gary J., Fian, Carina, Homayouni, Yasaman, Ilić, Dragana, Kaspi, Shai, Kovačević, Andjelka B., Landt, Hermine, Č. Popović, Luka, Storchi-Bergmann, Thaisa, Wang, Jian-Min and Zaidouni, Fatima

It is advisable to refer to the publisher's version if you intend to cite from the work.
https://doi.org/10.3847/1538-4357/ad8160

For information about Research at UCLan please go to http://www.uclan.ac.uk/research/

All outputs in CLoK are protected by Intellectual Property Rights law, including Copyright law. Copyright, IPR and Moral Rights for the works on this site are retained by the individual authors and/or other copyright owners. Terms and conditions for use of this material are defined in the http://clok.uclan.ac.uk/policies/

The Astrophysical Journal, 976:59 (19pp), 2024 November 20 https://doi.org/10.3847/1538-4357/ad8160
© 2024. The Author(s). Published by the American Astronomical Society.
OPEN ACCESS

AGN STORM 2. X. The Origin of the Interband Continuum Delays in Mrk 817*

Hagai Netzer[1], Michael R. Goad[2], Aaron J. Barth[3], Edward M. Cackett[4], Keith Horne[5], Chen Hu[6], Erin Kara[7], Kirk T. Korista[8], Gerard A. Kriss[9], Collin Lewin[7], John Montano[3], Nahum Arav[10], Ehud Behar[7,11], Michael S. Brotherton[12], Doron Chelouche[13,14], Gisella De Rosa[9], Elena Dalla Bontà[15,16,17], Maryam Dehghanian[10], Gary J. Ferland[18], Carina Fian[19,20], Yasaman Homayouni[9,21,22], Dragana Ilić[23,24], Shai Kaspi[25], Andjelka B. Kovačević[23], Hermine Landt[26], Luka Č. Popović[23,27], Thaisa Storchi-Bergmann[28], Jian-Min Wang[6,29,30], and Fatima Zaidouni[7]

[1] School of Physics and Astronomy, Tel Aviv University, Tel Aviv 6997801, Israel
[2] School of Physics and Astronomy, University of Leicester, University Road, Leicester, LE1 7RH, UK
[3] Department of Physics and Astronomy, 4129 Frederick Reines Hall University of California, Irvine, CA 92697-4575, USA
[4] Department of Physics and Astronomy, Wayne State University, 666 W. Hancock Street, Detroit, MI 48201, USA
[5] SUPA School of Physics and Astronomy, North Haugh, St. Andrews, KY16 9SS, Scotland, UK
[6] Key Laboratory for Particle Astrophysics, Institute of High Energy Physics, Chinese Academy of Sciences, 19B Yuquan Road, Beijing 100049, People's Republic of China
[7] MIT Kavli Institute for Astrophysics and Space Research, Massachusetts Institute of Technology, Cambridge, MA 02139, USA
[8] Department of Physics, Western Michigan University, 1120 Everett Tower, Kalamazoo, MI 49008-5252, USA
[9] Space Telescope Science Institute, 3700 San Martin Drive, Baltimore, MD 21218, USA
[10] Department of Physics, Virginia Tech, Blacksburg, VA 24061, USA
[11] Department of Physics, Technion, Haifa 32000, Israel
[12] Department of Physics and Astronomy, University of Wyoming, Laramie, WY 82071, USA
[13] Department of Physics, Faculty of Natural Sciences, University of Haifa, Haifa 3498838, Israel
[14] Haifa Research Center for Theoretical Physics and Astrophysics, University of Haifa, Haifa 3498838, Israel
[15] Dipartimento di Fisica e Astronomia "G. Galilei," Università di Padova, Vicolo dell'Osservatorio 3, I-35122 Padova, Italy
[16] INAF—Osservatorio Astronomico di Padova, Vicolo dell'Osservatorio 5, I-35122, Padova, Italy
[17] Jeremiah Horrocks Institute, University of Central Lancashire, Preston, PR1 2HE, UK
[18] Department of Physics and Astronomy, The University of Kentucky, Lexington, KY 40506, USA
[19] Departamento de Astronomía y Astrofísica, Universidad de Valencia, E-46100 Burjassot, Valencia, Spain
[20] Observatorio Astronómico, Universidad de Valencia, E-46980 Paterna, Valencia, Spain
[21] Department of Astronomy and Astrophysics, The Pennsylvania State University, 525 Davey Laboratory, University Park, PA 16802, USA
[22] Institute for Gravitation and the Cosmos, The Pennsylvania State University, University Park, PA 16802, USA
[23] University of Belgrade—Faculty of Mathematics, Department of Astronomy, Studentski trg 16, 11000 Belgrade, Serbia
[24] Hamburger Sternwarte, Universität Hamburg, Gojenbergsweg 112, 21029 Hamburg, Germany
[25] School of Physics and Astronomy and Wise Observatory, Tel Aviv University, Tel Aviv 6997801, Israel
[26] Centre for Extragalactic Astronomy, Department of Physics, Durham University, South Road, Durham, DH1 3LE, UK
[27] Astronomical Observatory, Volgina 7, 11060 Belgrade, Serbia
[28] Departamento de Astronomia—IF, Universidade Federal do Rio Grande do Sul, CP 150501, 91501-970 Porto Alegre, RS, Brazil
[29] School of Astronomy and Space Sciences, University of Chinese Academy of Sciences, 19A Yuquan Road, Beijing 100049, People's Republic of China
[30] National Astronomical Observatories of China, 20A Datun Road, Beijing 100020, People's Republic of China
Received 2024 August 2; revised 2024 September 20; accepted 2024 September 25; published 2024 November 13

Abstract

The local ($z = 0.0315$) active galactic nucleus (AGN) Mrk 817 was monitored over more than 500 days with space-borne and ground-based instruments as part of a large international campaign, AGN STORM 2. Here, we present a comprehensive analysis of the broadband continuum variations using detailed modeling of the broad line region (BLR), several types of disk winds classified by their optical depth, and new numerical simulations. We find that diffuse continuum (DC) emission, with additional contributions from strong and broad emission lines, can explain the continuum lags observed in this source during high- and low-luminosity phases. Disk illumination by the variable X-ray corona contributes only a small fraction of the observed continuum lags. Our BLR models assume radiation-pressure-confined clouds distributed over a distance of 2–122 light days. We present calculated mean emissivity radii of many emission lines, and DC emission, and suggest a simple, transfer-function-dependent method that ties them to cross-correlation lag determinations. We do not find clear indications for large-optical-depth winds, but identify the signature of lower-column-density winds. In particular, we associate the shortest observed continuum lags with a combination of $\tau(1\ \mathrm{Ryd}) \approx 2$ wind and a partly shielded BLR. Even smaller optical depth winds may be associated with X-ray absorption features and with noticeable variations in the widths and lags

* Based in part on observations associated with program GO-16196 made with the NASA/ESA Hubble Space Telescope, obtained at the Space Telescope Science Institute, which is operated by the Association of Universities for Research in Astronomy, Inc., under NASA contract NAS5-26555.

Original content from this work may be used under the terms of the Creative Commons Attribution 4.0 licence. Any further distribution of this work must maintain attribution to the author(s) and the title of the work, journal citation and DOI.

of several high-ionization lines like He II and C IV. Finally, we demonstrate the effect of torus dust emission on the observed lags in the i and z bands.

Unified Astronomy Thesaurus concepts: Galaxy accretion disks (562); Supermassive black holes (1663); Emission line galaxies (459); Reverberation mapping (2019); Active galactic nuclei (16)

1. Introduction

Active galactic nuclei (AGNs) are known for their very high luminosity, originating from the vicinity of the supermassive black hole at their center, and for their highly variable continuum and emission lines. Two types of studies aimed at understanding the nature of these variations have been carried out over several decades. One type involves high-cadence monitoring of a large number of AGNs in a small number of UV and optical bands (see, e.g., S. Kaspi et al. 2000; M. C. Bentz et al. 2013; Y. Shen et al. 2016; P. Lira et al. 2018; P. Du & J.-M. Wang 2019). Such reverberation mapping (RM) campaigns reveal a strong correlation between the variation of the hydrogen Balmer lines and the optical continuum, where the line flux follows the continuum flux with luminosity- and Eddington-ratio-dependent lags. Similar luminosity-dependent correlations between C IV and other strong emission lines and the UV/optical continuum have also been found. Such correlations have become a standard tool for measuring the black hole (BH) mass in AGNs at all redshifts and luminosities.

A second type of campaign is the long-term multiwavelength monitoring of individual sources to find luminosity-dependent lags between different bands or between emission lines and continuum bands. Some studies focus on broadband observations, looking for a luminosity-dependent correlation between X-ray and UV or X-ray and optical variations (e.g., the large Fairall-9 campaign described in J. V. Hernández Santisteban et al. 2020). While statistically significant correlations between the X-ray and optical continua are hard to find, strong correlations between several optical and UV continuum bands are widespread. Among the most successful long-term spectroscopic studies, we mention the 2014 AGN STORM 1 campaign, which aimed to monitor the X-ray to infrared continuum and emission-line variations in NGC 5548 (G. De Rosa et al. 2015; M. M. Fausnaugh et al. 2016; L. Pei et al. 2017).

AGN STORM 2 is a large monitoring campaign that follows a local ($z = 0.0315$) AGN, Mrk 817, over a period that has already exceeded 500 days. The project combines spectroscopic and photometric data in several wavelength bands, from infrared to hard X-rays. The telescopes and instruments involved are the Hubble Space Telescope (HST) COS and STIS spectrographs, SWIFT, XMM, NuStar, NICER, and several small-to-medium-size ground-based telescopes. The observations show large-amplitude X-ray and UV variations and smaller variations at longer wavelengths. So far, the project has resulted in nine published and submitted papers: E. Kara et al. (2021), E. M. Cackett et al. (2023, hereafter, C23), E. R. Partington et al. (2023), Y. Homayouni et al. (2023, 2024), F. Zaidouni et al. (2024), J. M. M. Neustadt et al. (2024), M. Dehghanian et al. (2024), and C. Lewin et al. (2024, hereafter, L24).

Spectroscopic RM analysis based on AGN STORM 2 published and unpublished data (C. Hu, private communication) suggests a lag of about 25 ± 5 days between the 5100 Å continuum and the Hβ line, depending on the exact part of the continuum light curve used in the analysis. There are also measured lags between the C IV emission line and the UV continuum, which change between 3 and 12 days throughout the campaign (see Y. Homayouni et al. 2024). Broadband photometry—combining HST, SWIFT, and ground-based facilities—suggests lags relative to the HST/1144 Å rest wavelength continuum that increase with wavelength, from about 2 days for the 2000–4000 Å continuum to more than 4 days in the i and z bands (see C23; L24). The X-ray to UV variations are hard to interpret, and no clear lags persisting over long periods have been found. Some papers address temperature variations across the accretion disk (J. M. M. Neustadt et al. 2024). Still, it is not yet clear what the connection, if any, is between this study and the total size and geometry of the disk.

The present paper aims to use detailed photoionization modeling of radiation-pressure-confined (RPC) clouds (A. Baskin et al. 2014; J. Stern et al. 2014; A. Baskin & A. Laor 2018; H. Netzer 2020) in the broad line region (BLR) of Mrk 817 to test the suggestion that the time-variable diffuse emission from this region is the primary source of the observed optical/UV broadband lags. Models of this type have already been applied to other local AGNs (e.g., H. Netzer 2022). However, previous attempts did not investigate the physics of the BLR gas and the properties of the disk wind (DW) observed in this source at such a level of detail. In particular, we try to explain the observed broadband line and continuum variations by combining time-dependent emission from an X-ray-illuminated disk with the variable diffuse continuum (DC) flux from the BLR. We use the models to address the size of the accretion disk and the geometry of the BLR in Mrk 817.

Section 2 of the paper provides information about the variability observed in this source. In Section 3, we present our combined disk–BLR model, and in Section 4 we present new numerical simulations that enable us to predict the expected continuum lags using a simple, easy-to-calculate expression. The results are shown and discussed in Section 5, where we also present a comprehensive analysis of various types of DWs observed in this source. Additional minor but important issues are discussed in the appendices. Throughout the paper, we assume a luminosity distance $d_{\rm L} = 134.2$ Mpc for Mrk 817[31] and cosmological parameters $H_0 = 72$ km s^{-1} Mpc^{-1} , $\Omega_\Lambda = 0.7$, and $\Omega_M = 0.3$.

2. Observations and Basic Assumptions

2.1. Continuum Spectral Energy Distribution

We used the multiwavelength observations of Mrk 817 described in earlier papers about AGN STORM 2 to construct a combined X-ray disk–BLR model for this source. The model follows the computations of O. Slone & H. Netzer (2012). It assumes an optically thick, geometrically thin accretion disk around a BH of mass $M_{\rm BH} = 4 \times 10^7 M_\odot$ and spin parameter $a = 0.7$, which corresponds to a mass conversion efficiency of $\eta = 0.1$. Full relativistic corrections and Comptonization are included in the calculations. The disk spectrum was combined

[31] See http://www.astro.gsu.edu/AGNmass/.

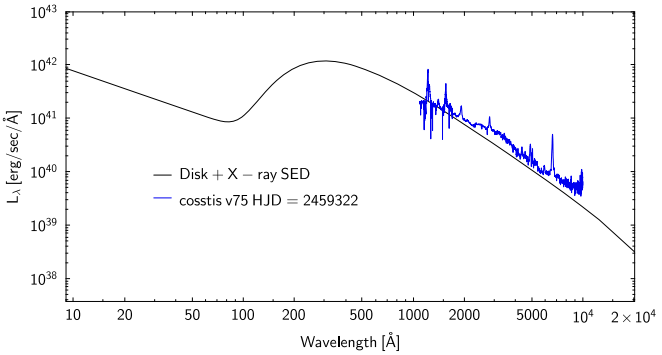

Figure 1. Assumed continuum SED (in black) for Mrk 817 constructed from a thin disk and a power-law X-ray source normalized to the luminosity during the first 100 days of the campaign. The disk inclination to the line of sight is given by $\cos i = 0.75$. The blue line is a COS-STIS spectrum obtained on the HJD marked in the figure. More details are provided in the text.

with a power-law $\Gamma = 1.9$ X-ray source normalized to the disk 2500 Å luminosity, such that $\alpha_{OX} = -1.45$. The combination of the two assumes that the source of the emitted X-ray radiation is disk accretion. Thus, the X-ray luminosity is part of the bolometric luminosity of the system. Given the small contribution of the X-ray luminosity to $L_{\rm bol}$ (about 10%), the angular dependence of the X-ray radiation is not very important, and complete isotropy was assumed.

The present spectral energy distribution (SED) is normalized differently from the one presented by E. Kara et al. (2021). It considers the disk inclination to the line of sight, i, which is chosen to be $\cos i = 0.75$. This issue was discussed in earlier campaign papers (e.g., F. Zaidouni et al. 2024), and inclination angles as small as 20° have been suggested. Here, we assume a standard limb-darkening law of $L_\nu \propto \cos i(1 + b\cos i)$ with $b = 2$ (e.g., H. Netzer 2013) to obtain the bolometric luminosity of the disk.

A major assumption of the models described below is a large DC contribution to all wavelengths between 1800 and 10000 Å. The luminosity normalization is based on a combined HST/COS-STIS (hereafter COS-STIS) spectrum obtained on HJD = 2459322. This spectrum is similar to the COS-STIS spectrum obtained on HJD = 2459202, shown and discussed in E. Kara et al. (2021). We assume no contribution from the host galaxy to this spectrum at all observed wavelengths, because of the narrow entrance aperture (0.″1). Given all this, the models in H. Netzer (2022) as well as the new models presented in this paper, the normalized disk spectrum at the beginning of the campaign is taken to be $\lambda L_\lambda(5100\,\text{Å}) = 5.3 \times 10^{43}\,\text{erg s}^{-1}$, and the DC contribution at 5100 Å is about 20%–30%. The bolometric disk luminosity is $6 \times 10^{44}\,\text{erg s}^{-1}$, which gives $L/L_{\rm edd} \approx 0.1$, about a factor of 1.8 smaller than the one assumed in several previous publications from the campaign. The total observed disk+X-ray luminosity at HJD = 2459322 is about $9.8 \times 10^{44}\,\text{erg s}^{-1}$, which differs from the bolometric luminosity due to the disk inclination. The photoionization calculations described below assume that this is also the total luminosity seen by the BLR gas and the DW described below. The assumed disk+X-ray SED and the COS-STIS spectrum are shown in Figure 1.

2.2. Variability

2.2.1. Lag Measurements

This work aims to analyze various observed situations involving the mixing of two sources of lags: X-ray illumination and variable BLR and DW emission. The HST/SWIFT data and the derived lags are described in C23 and L24. Additional ground-based data in the *u, g, r, i,* and *z* bands are taken from Tables 1 and 2 in L24 and from the analysis of the AGN STORM 2 ground-based photometric campaign by J. Montano (2024, in preparation). We also use our own interpolated cross-correlation function (ICCF) lag measurements, using data from C23.

The C23 results and our measurements were derived from the computed ICCF (e.g., B. M. Peterson 2007), with no detrending or smoothing of the light curves. The L24 lags are the results of frequency-resolved analysis (P. Uttley et al. 2014) and thus depend on the chosen range of frequency (given in units of inverse days). The differences between the two approaches are minor for the lowest-frequency bin used by L24, which corresponds to 50–100 days. The differences increase at higher frequencies that correspond to shorter and shorter periods. In particular, the so-called "Epoch 1" and "Epoch 2" lags discussed in L24 were derived from a higher-frequency bin corresponding to 20–70 days. They should not be directly compared with the ICCF-derived lags. The shortening lags with increasing frequency are similar to the decreasing lags caused by light-curve detrending.

All lags listed in L24 were measured relative to the SWIFT/UVW2 band. Since we are after the lags relative to the ionizing continuum flux, we remeasured the lag of the UVW2 band relative to the 1144 Å rest-wavelength continuum, which we used as a proxy for the light curve of the ionizing radiation. This lag depends slightly on the 1144 Å flux. Over the first 200 days of the campaign, it is roughly 0.6 days. This is identical to the lag of 0.66 days measured by C23 within the uncertainties. As shown below, additional lags between the 1144 Å band and the ionizing flux are also important.

2.2.2. Changing SED

C23 conducted a flux–flux analysis to remove nonvariable and long-term variable components from the observed spectra. The method assumes no wavelength-dependent variations in the intrinsic disk SED. Given this assumption, they show that the shape of the variable SED (which includes the disk and diffuse BLR emission) is consistent with SEDs of optically thick, geometrically thin accretion disks.

A more detailed examination of the available COS-STIS spectra obtained during times of high and low 1144 Å flux does not meet this assumption. This is illustrated in Figure 2, where we show COS-STIS spectra from HJD = 2459322 (a high flux level) and HJD = 2459421 (a very low flux level). Given the negligible contribution of the host galaxy to these spectra, due to the 0.″1 slit width of the HST instruments and the similarity of the two spectra at long wavelengths, it is evident that the fractional variations at short wavelengths are larger than those observed at long wavelengths. This is illustrated in the difference spectrum shown in the figure. The difference cannot be caused by DC emission from the BLR, which is very small at short wavelengths around 1144 Å and amounts to only 20%–30% at long wavelengths.

There are several possible ways to explain the significant change in SED shape illustrated in Figure 2. The first is an additional nuclear source, with a diameter not exceeding 70 pc, which contributes a significant fraction of the observed flux, especially at long wavelengths, at times of low AGN luminosity. A compact nuclear star cluster is one such

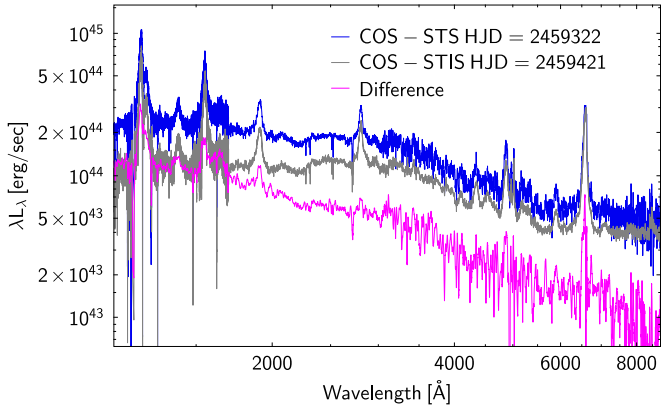

Figure 2. A comparison of two COS-STIS spectra obtained during periods of high (v75, HJD = 2459322) and low (v30, HJD = 2459421) 1144 Å flux levels. The magenta curve shows the difference between the two spectra. The similarity of the spectra at long wavelengths compared with a factor of ≈2 difference in the 1144 Å flux suggests a significant change in the shape of the SED between the two epochs.

possibility. However, we are unaware of a similar case among local AGNs, especially those whose surface brightness profile was separated into AGN and stellar-light components at HST resolution, as was done for this source (M. C. Bentz et al. 2009). This possibility should be further investigated by looking at the expected spectral characteristics of such clusters, which is beyond the scope of the present paper. A second possibility is an intrinsic change in SED shape, which makes the disk bluer when it is brighter. This has been observed in detailed observations of nearby AGNs like NGC 5548 (W. Wamsteker et al. 1990; D. Maoz et al. 1993; K. T. Korista et al. 1995) and in hundreds of low- and high-redshift AGNs (D. E. Vanden Berk et al. 2004; Y.-H. Sun et al. 2014), although other interpretations have also been proposed (J. R. Weaver & K. Horne 2022).

The second possibility mentioned above means that the galaxy light inside the 5″ radius SWIFT aperture derived in a flux–flux analysis overestimates the real flux in the *B* and *V* bands by large factors (for the general limitations of the method, see M. Cai et al. 2024). An estimate of the excess galaxy flux is obtained by comparing the galaxy flux in the C23 *B* and *V* bands with the measured COS-STIS fluxes. This suggests an overestimate of ≈3.1 in the *B* band and a factor of ≈2.7 in the *V* band. We can also compare the deconvolved *V*-band galaxy flux in M. C. Bentz et al. (2009) with the result of the flux–flux analysis. Given the factor of 2.07 in aperture size between the two observations, this suggests galaxy *V*-band flux inside the SWIFT aperture, which is very close to the one derived from the COS-STIS/SWIFT comparison. Given this, the changing-SED-shape interpretation is adopted for the rest of this paper, and we leave a more elaborate analysis for future publications.

Finally, we fitted the fainter COS-STIS spectrum using a thin-accretion-disk SED with a mass accretion rate of 0.05 $M_{\odot}\,\mathrm{yr}^{-1}$, which is half of our canonical accretion rate. The lower-accretion-rate disk reasonably fits the short-wavelength SED but underestimates the long-wavelength part. Such a low accretion rate can change the ionization level nonlinearly. All BLR models presented below assume the SED shown in Figure 1, and a more detailed analysis of this issue is beyond the scope of the present paper.

3. BLR

3.1. RPC BLR Models

Published multi-cloud BLR models that calculate full, multiline BLR spectra can be divided into three generic types: constant-external-pressure models (see, e.g., M. J. Rees et al. 1989; M. R. Goad et al. 1993; S. Kaspi & H. Netzer 1999; M. C. Bottorff et al. 2000; D. Lawther et al. 2018), locally optimally emitting cloud models (J. Baldwin et al. 1995; K. Korista et al. 1997; K. T. Korista & M. R. Goad 2000, 2019; M. R. Goad & K. T. Korista 2015), and RPC cloud models (A. Baskin et al. 2014; A. Baskin & A. Laor 2018; H. Netzer 2020). The recent dusty wind calculations of Czerny, Naddaf, and collaborators (e.g., M. H. Naddaf et al. 2023 and references therein) focus on cloud dynamics and not on full models of individual sources. Here, we consider only RPC models and follow the procedures explained in detail in H. Netzer (2020, 2022).

RPC clouds are formed where the external radiation pressure, due to the incident AGN continuum, exceeds the gas pressure in the gas, and the photoionized gas clouds are not accelerated outward; i.e., the RPC model is a 1D (slab) hydrostatic solution for the photoionized gas. No outward acceleration can result from either a thick layer of neutral gas at the back of the cloud or a situation where the radiation momentum is absorbed by the ram pressure of a stationary, low-density medium. RPC clouds are not found where the gas pressure is larger than the external radiation pressure or where the gas is accelerated outward. We assume that there are very few if any such clouds in the BLR.

The important characteristic of RPC clouds is the distance-independent ionization parameter at the ionization front inside the clouds. Because of this, low and high ionization lines are produced over a very large range of distances in the BLR. All our photoionization models were calculated using version 17.02 of the code Cloudy (G. J. Ferland et al. 2017), following the exact procedure described in H. Netzer (2020).

The parameters for our RPC model are the central SED, the gas metallicity, the turbulent velocity inside the clouds, the column density and covering factor of the clouds, the inner and outer boundaries of the BLR, $R_{\rm in}$ and $R_{\rm out}$, and the cloud distribution between the two boundaries. The inner and outer boundaries determine the lags of the emission lines and the DC emission relative to the varying ionizing flux. These are the most important observational constraints on the model.

The overall geometry determines several of the RPC model parameters. $R_{\rm in}$ depends on the dimensions and physics of the central accretion disk. For a rotating gravitationally bound cloud system, the minimal $R_{\rm in}$ is approximately the self-gravity radius of the disk, which is of order $1000R_{\rm g}$, where $R_{\rm g}$ is the gravitational radius of the BH. Unbound DWs can originate closer to the BH and, while not part of the classical BLR, can produce observable emission and absorption features. $R_{\rm out}$ depends on the temperature of the nuclear dust, which, following earlier studies (H. Netzer 2015 and references therein), is assumed to take the shape of a massive small dusty torus whose inner walls contain pure graphite grains. Observations of many AGNs suggest that the distance to the inner walls of the dusty torus (the graphite grains sublimation radius) is about three to four times the mean emissivity radius (MER) of the hydrogen Balmer lines (e.g., GRAVITY Collaboration et al. 2020). For Mrk 817, this corresponds to a distance of about 100

light days. Given all this, and the observations described in E. Kara et al. (2021) and Y. Homayouni et al. (2024), the overall range of radii is assumed to be limited to $\log R(\mathrm{cm}) = 15.75 - 17.5$ (∼2–120 light days). We also assume a similar inclination of the thin central accretion disk and the thick flaring-disk BLR. The choice of $\cos i = 0.75$ is essential for calculating the observed versus intrinsic disk flux, the emission-line widths, and the transfer function (TF) of the BLR gas.

Below, we focus on three specific BLRs with different distances from the central BH. Model 1, indicated in all figures by green lines, represents either the innermost part of the BLR or a DW with $\log R(\mathrm{cm}) = 15.75 - 16$ (∼2–4 light days). The DW properties are also discussed in Section 5.4.1. The geometry, inclination, and gas velocity of the DW gas can differ substantially from that of the flaring-disk BLR. Model 2, indicated in blue, is an extended gravitationally bounded BLR with $\log R(\mathrm{cm}) = 16 - 17.25$ (∼4 – 70 light days). Model 3 (red lines) is similar to Model 2, except that the entire BLR is shifted to larger radii, $\log R(\mathrm{cm}) = 16.25 - 17.5$ (∼7–120 light days). We also calculated an additional model (Model 2a) with the same geometry and SED as Model 2 but half the bolometric luminosity. This is used to address the issue of line and continuum lags during phases of high and low luminosity and is discussed in Section 5.2.

All our models assume solar metallicity gas and an internal microturbulent velocity of $30\,\mathrm{km\,s^{-1}}$. Justification for this choice is discussed in H. Netzer (2020, 2022). The column density of the clouds in all three models is $N_{\mathrm{H}} = 10^{23.5}\ \mathrm{cm^{-2}}$, which is large enough to ensure that the total mass of individual clouds is dominated by neutral gas at the nonilluminated part of the cloud. A slight deviation from this assumption is discussed in Section 5.4. All models in this paper assume a side view of the emitting clouds, i.e., our line of sight to the central disk is not obscured by clouds. A factor not included in the present calculations is the anisotropy of optically thick line emission, particularly the Balmer lines. For the implications of this assumption, see P. T. O'Brien et al. (1994) and S. A. Rosborough et al. (2024).

The covering-factor dependence on distance in our BLR models, $C(R)$, is a crucial parameter. It is given by $dC(R) \propto R^{-\beta} dR$ and the integrated covering factor is fixed by the equivalent width of the strong UV lines and, as we show later, by the intensity of the DC. In most models shown here, $C(R_{\mathrm{out}}) = 0.2$. This "net covering factor" can be smaller than the geometrical covering factor determined by the opening angle of the flaring-disk BLR. We have experimented with several values of β in the range 1.8–2.4, shown in H. Netzer (2020), as the range required to explain the typical observed lags of several strong emission lines. $\beta = 2.4$ provides a somewhat better agreement with the lag measurements of several local AGNs. In all models shown here, $\beta = 2$.

3.2. Comparison with the Observed Spectra

Our RPC BLR models should be considered representative of many Type I AGNs. We ensured that they generally agree with the observed spectra of Mrk 817, especially with the measured lags of the strong emission lines, and can be used to estimate reliable continuum time delays. We did not attempt to calculate accurate velocity-dependent lags of all the strong emission lines, since such calculations require specific treatment of the amplitude and variability pattern of the driving

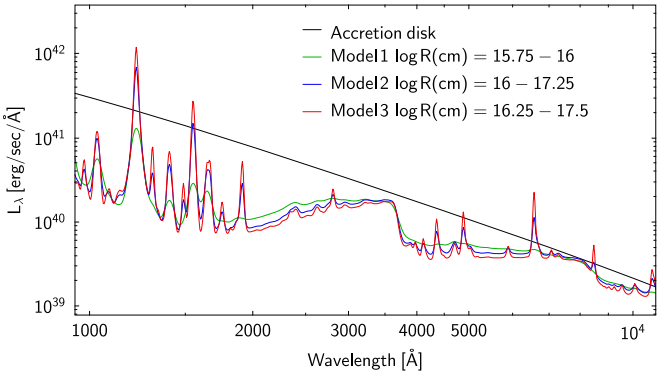

Figure 3. Calculated spectra of three BLR models considered in this paper with $C(R_{\mathrm{out}}) = 0.2$. The inner and outer boundaries are marked inside the figure. Note the significant differences in the emission-line widths reflecting the different distances from the central BH. In particular, in Model 1 (green line), significant velocity broadening makes line emission hard to discern.

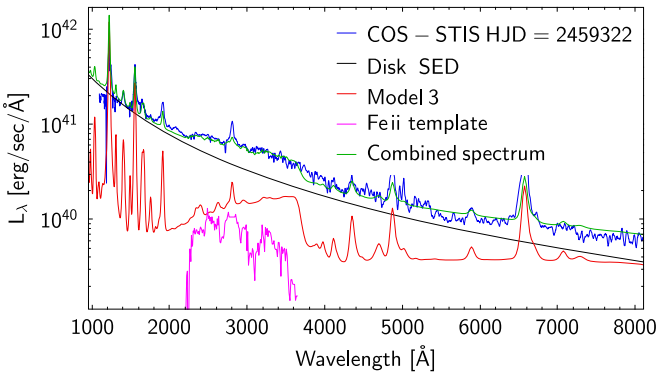

Figure 4. Comparison of the COS-STIS spectrum with an empirical model (green line) made of two components: Model 3 from Figure 3 (red line) and the Fe II template based on the UV observations of J. E. Mejía-Restrepo et al. (2016; magenta line).

continuum light curve. Not all the data required for such modeling are available for Mrk 817, and the calculated continuum delay, the center of this paper, does not depend much on the emission-line model.

Figure 3 shows the assumed disk continuum and the calculated spectra of the three generic models. An important feature is that the fraction of diffuse emission is never smaller than about 10% of the incident flux, even at the shortest wavelength shown, at around 1100 Å. As explained below, this is important for fixing the zero-lag point in broadband RM observations.

We compare Model 2 and Model 3 with the COS-STIS spectrum discussed in Section 2. We focus on Model 3, which we show later as our preferred model for explaining the observed continuum lags. The comparison is shown in Figure 4. There is good agreement over much of the 1000–9000 Å spectral range, including the strong UV emission lines and the DC at wavelengths larger than 4000 Å. The model fails in two important ways. The first is a well-known yet unsolved problem in modeling the broad Balmer line emission of Type I AGNs (see, e.g., H. Netzer 2020 and references therein). This extends also to the high-n lines in the Balmer series (see the deficit flux at around 3800 Å) and has been investigated in several earlier publications (e.g., B. J. Wills et al. 1985; J. Kovacevic et al. 2014). The second is related to the failure of standard photoionization models to calculate the

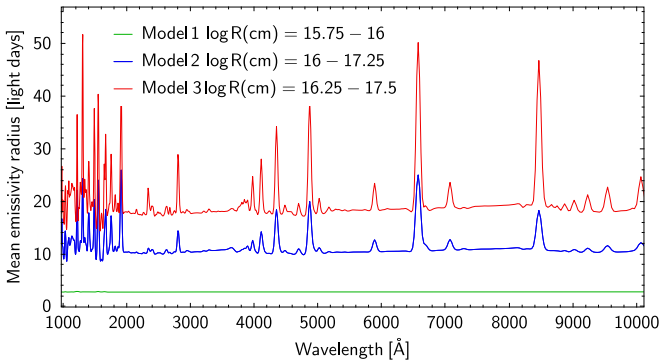

Figure 5. MERs as a function of wavelength for the three BLR models shown in Figure 3.

intensities of Fe II lines over the 2000–4000 Å range. This has been discussed in numerous publications (e.g., B. J. Wills et al. 1985; J. E. Mejía-Restrepo et al. 2016; L. Č. Popović et al. 2019; D. Ilic et al. 2023), where various empirical recipes were provided to improve the fits of the data. We artificially added the missing Fe II flux to Figure 4 (see the figure caption), but not the high-order Balmer lines or the optical Fe II lines. Such additions will make the overall agreement between the model and observations much better, but they do not mean much, given the fundamental failure of the models. In the time-lag calculations discussed below, we neglect the Fe II lines shown in Figure 4.

3.3. MER

Figure 5 shows the MERs of the three BLR models calculated in this paper. There is a clear difference between the MERs of various broad emission lines, which depend mainly on their different locations. The MER of the DC, which represents primarily bound–free continua with little contribution from free–free emission, is almost wavelength-independent. We also include Rayleigh scattering from neutral hydrogen, which in the RPC model is seen as very broad and weak Ly-α line wings.

Several bands used in the observations include individual emission lines and DC emissions. In such cases, one can define three somewhat different MERs. In principle, the MER of a single isolated emission line can be recovered by RM campaigns in cases where the duration of the driving continuum pulse is at least as long as the crossing time of the line-emitting region (in reality, this is hard to achieve, as explained in the numerical simulations part in Section 4). This MER refers to the total line flux. Velocity-resolved lags, when available, provide MERs for every velocity component, provided the line emission can be separated from the underlying DC emission. The third type of MER is important when using broadband observations that combine line and DC emission. Time lags based on such observations differ from the other two types of MERs. For example, a broadband measurement of Hβ together with the 4861 Å Paschen continuum emission will result in a lag that is shorter than the measured lag of Hβ, since the MER of the DC is about half the MER of the strong Balmer lines. This situation is illustrated in Figure 15 in Appendix A. As discussed in the simulation section below, RM campaigns hardly ever result in lags that are longer than about 80% of the crossing time of the MER. For the 1144 Å driving continuum used here, the number is closer to 70%. These numbers are listed as footnotes in Table 1.

Table 1
MERs in Light Days and Predicted and Observed Lags in Days

Model	1[a]	2[b]	3[b]
Hβ MER	2.8	24.1	38
Hβ predicted lag	2.5	15	25
Hβ observed lag[c]	24	24	24
C IV MER	2.8	18.8	31
C IV predicted lag	2.5	12.2	20.1
C IV observed lag[d]	12	12	12
He II MER	2.8	11.0	20.7
He II predicted lag	2.5	7.2	13.5
He II observed lag[d]	9	9	9
DC MER	2.8	11.2	19
DC predicted lag	2.5	7.3	10.4

Notes.
[a] Predicted lag = MER × 0.9.
[b] Predicted lag = MER × 0.65.
[c] E. Kara et al. (2021).
[d] Y. Homayouni et al. (2023).

The calculated lags for the total Hβ and C IV emission lines in Mrk 817, in Model 2 (24 and 16 days, respectively), agree with the results of E. Kara et al. (2021). Note also that the outer radius in this model is about three times the MER of the Hβ line. All predicted line lags in Model 3 are also in reasonable agreement with the observations. These lags are roughly consistent with the canonical lags observed in low-Eddington-ratio AGNs (e.g., P. Lira et al. 2018; P. Du & J.-M. Wang 2019). However, Model 1 predicts much shorter lags that agree with some C IV lag measurements but not with others (e.g., Y. Homayouni et al. 2024). As shown below, this is the main reason for the association of this model with a DW.

3.4. Combined Disk–BLR Models

The basic assumption in this paper is that the measured broadband UV/optical lags are combinations of short lags of order 0.5–2 days, from an X-ray-illuminated disk, with longer lags typical of BLR emission. A rigorous way to combine the two is to calculate TFs, or response functions, which combine the BLR and disk emission. This is tricky, since every line in the BLR has a different TF, and some line emission is mixed with a DC emission with additional TFs. Earlier papers have tried this idea using a generic TF representing a "typical" BLR response. One such case is presented in L24. As shown in Appendix B, this assumed TF disagrees with the DC TF computed here.

Here, we adopt a time-domain forward-modeling approach that was tested successfully in earlier studies of other AGNs. The combined disk–BLR lag, which does not include delays due to thermal dust emission (to be treated later), is a wavelength-dependent expression given by

$$\tau_{\lambda,\mathrm{tot}} = \tau_{\lambda,\mathrm{irr}}\left[\frac{L_{\mathrm{inc}}}{L_{\mathrm{tot}}}\right] + f_{\mathrm{lag}}\,(\mathrm{TF}) \times \tau_{\lambda,\mathrm{diff}}\left[\frac{L_{\mathrm{diff}}}{L_{\mathrm{tot}}}\right]\ \mathrm{days}, \quad (1)$$

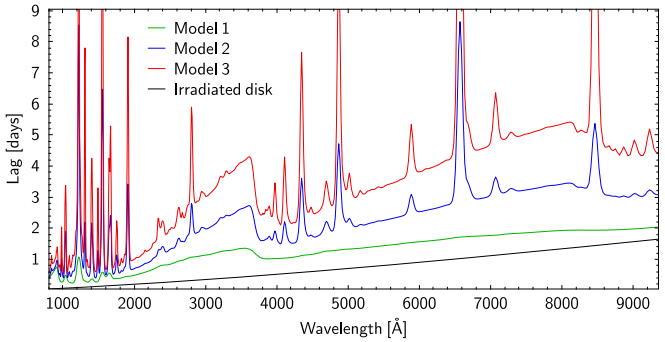

Figure 6. Computed continuum lags for the three models shown in Figure 3, assuming $f_{\rm lag} = 0.9$ for Model 1 and $f_{\rm lag} = 0.5$ for the other two models (see the text for the justification). The large differences in lags mostly reflect the different MERs of the models.

where $\tau_{\lambda,\rm irr}$ and $\tau_{\lambda,\rm diff}$ are the lags due to the illuminated disk and the diffuse BLR emission, respectively; $L_{\rm inc}$ is the luminosity of the incident continuum; $L_{\rm diff}$ is the diffuse (BLR) luminosity that includes DC and broad emission lines; $L_{\rm tot} = L_{\rm diff} + L_{\rm inc}$; and $f_{\rm lag}$(TF) is a correction factor that depends on the TF and nature of the driving light curve. The above expression, with $f_{\rm lag}({\rm TF}) = 1$, is taken from H. Netzer (2022), and similar earlier expressions are discussed in e.g., D. Lawther et al. (2018) and J. V. Hernández Santisteban et al. (2020). The numerical simulations below show that the best value for Models 2 and 3 is $f_{\rm lag}({\rm TF}) = 0.5$.

The total time lag calculated in this way, $\tau_{\lambda,\rm tot}$, should be compared either with the lags measured in the lowest-frequency bins in the frequency-resolved analysis of E. M. Cackett et al. (2022) and L24 or the lags measured with the ICCF method for nondetrended LCs. The disk–lag term, $\tau_{\lambda,\rm irr}$, is given by Equation (1) of H. Netzer (2022) and is basically identical to Equation (12) in M. M. Fausnaugh et al. (2016). It assumes $X = 2.49$, $L_x/L_{\rm disk} = 0.1$, $h = 10R_{\rm g}$, a disk albedo of 0.2, and no relativistic corrections; all standard assumptions used in earlier calculations.

Figure 6 shows the computed lags for the three cases shown in Figure 3. The numerical simulations below show that the best estimates require $f_{\rm lag} = 0.9$ for Model 1 and $f_{\rm lag} = 0.5$ for Models 2 and 3. The total disk+BLR lags are very different at all wavelengths longer than about 1800 Å, reflecting the different MERs of the three models.

4. Simulations

4.1. The Dependence of the Measured Delay on DC Fractional Contribution

Before proceeding to use Equation (1), we want to estimate the effect on the measured delay of the differing diffuse emission contributions (assumed here to be only DC emission) of the total light, DC/(disk+DC), for our model BLR. The first step is to investigate the behavior of a simple toy model, in which effects due to geometric dilution of the input signal (resulting from a spatially extended BLR) are completely removed. This we achieve by modeling the response of a geometrically thin ring of gas located 10 light days from the continuum source and viewed face on. For this geometry, the response function may be represented by a delta function in time. Assuming a linear response approximation, the output signal from this thin ring of gas (the DC component) will be a copy of the input signal (the driving component, initially taken to be the 1144 Å continuum light curve for the full campaign), shifted in time by an amount equal to the light-crossing time to the region. The measured delay, as determined by cross-correlating the input signal with the output signal, will, in this instance, be precisely 10 days.

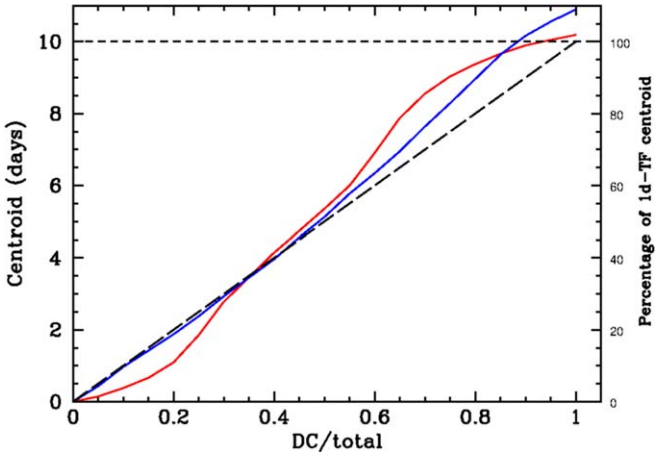

Figure 7. The measured delay (ICCF centroid) as a function of the DC fractional contribution to the total light (Disk+DC) for a face-on thin ring with a radius of 10 light days. The output signal is the sum of the input signal (driving light curve) and responding signal, such that the responding signal contributes a fraction of the total light in the range 0–1. The measured delay is taken to be the centroid of the cross-correlation function determined from cross-correlating the driving and responding signals (see the text for details). The dashed horizontal line indicates the delay of the DC component only (=10 days). The diagonal line indicates linearity—the measured delay is directly proportional to the fractional contribution of the DC component to the total light. Results are shown for two instances of the driving continuum light curve: the F(1144 Å) light curve for Mrk 817 (red) and a damped random walk, $T_{\rm dur} = 500$ days, and damping timescale, $T_{\rm char} = 40$ days (blue).

Next, we investigate the measured delay between the input signal and an output signal comprising the sum of the input signal and the responding DC component, such that the fractional contribution of the DC component to the total light is in the range 0–1. The delay is computed from the ICCF centroid, here determined for time intervals spanning values of the cross-correlation coefficient $>0.8 \times {\rm CCF}_{\rm peak}$, where ${\rm CCF}_{\rm peak}$ is the peak correlation coefficient.

The results from this study are shown in Figure 7, with the solid red line. As indicated in Figure 7, the measured delay, with respect to the input signal, increases as the fractional contribution of the DC component to the total light increases. However, the relationship, while approximately linear, is not strictly linear, even for this simple model, with the measured delay being biased toward the delay of the major contributory component. Since the measured delay also depends on the characteristic variability timescale $T_{\rm char}$ of the driving continuum relative to the size of the region being probed and the light curve duration (see Appendix D), a strictly linear dependence between the measured delay and DC fractional contribution may in practice never be realized. We have tested this behavior using simulated driving light curves of fixed duration but with different characteristic damping timescales. The measured lag dependence on DC fractional contribution for a face-on thin ring is close to linear at small DC fractional contributions if $T_{\rm char}$ is larger than the MER, provided that the light curve is of sufficient duration. Figure 7 shows an example simulation using a driving light curve with $T_{\rm dur} = 500$ days and

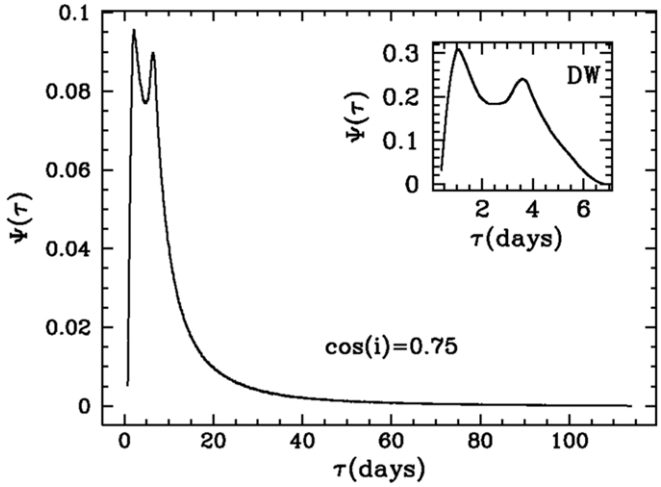

Figure 8. The 1D response function (or TF) for the 7995 Å continuum band, for our model BLR viewed at line-of-sight inclination $\cos(i) = 0.75$. The response function has been normalized to the unit area. Inset: the 1D response function for the 7995 Å continuum band arising from the DW (Model 1) viewed at the same inclination.

a damping timescale $T_{\rm char} = 40$ days (see Appendix D for details).

4.2. Mrk 817

For Mrk 817, we model the response of the DC band at 7995 Å arising from a BLR geometry here described as a geometrically thick flared disk, with inner radius $R_{\rm in} = 10^{16.0}$ cm, outer radius $R_{\rm out} = 10^{17.25}$ cm, semi-opening angle 11.°4, and differential radial covering fraction $dC(R) \propto R^{-2}dR$. The total covering fraction for this particular geometry, $C(R_{\rm out})$, is 0.2. The response function for the 7995 Å DC band for our adopted geometry viewed at a line-of-sight inclination $\cos(i) = 0.75$ is shown in Figure 8. The response function is double-peaked, characteristic of a flattened geometry, and is strongly peaked toward smaller delays, with a weak extended tail toward longer delays. The MER or, equivalently, the centroid of the response function for this continuum band is 11.26 days.

For the proxy driving continuum, we use the 1144 Å continuum band located shortward of Ly-α. We choose this band due to its proximity to the EUV continuum responsible for driving continuum and emission-line variations at longer wavelengths, and because at shorter wavelengths, far enough from the Rayleigh scattering feature beneath Ly-α, the DC contribution to the total light is small when compared to DC contributions at longer wavelengths. We use the part of the 1144 Å continuum LC extending from HJD = 2459177 to HJD = 2459377 (hereafter "window 1"). This covers the period from the beginning of window 1 to the end of "window 3," as defined in Y. Homayouni et al. (2024). We expect some dependence of the results from the simulations on our chosen window. As for our simple toy model, we drive the response of the DC band at 7995 Å with our proxy driving continuum and measure the delay between the driving continuum and DC band from the ICCF. The measured delay for the DC component only (=7.28 days) over the full campaign is ≈35% smaller than the model response function centroid for this band (=11.26 days). While the ICCF centroid is commonly taken to be representative of the emissivity-weighted radius (or equivalently response function centroid), previous studies have shown that this is rarely realized in practice (e.g., M. R. Goad and K. T. Korista 2014, 2015)—a combination of a mismatch between the characteristic timescale of the driving continuum and the BLR "size," the short campaign duration (see Appendix D), as well as the weak extended tail of the response function.

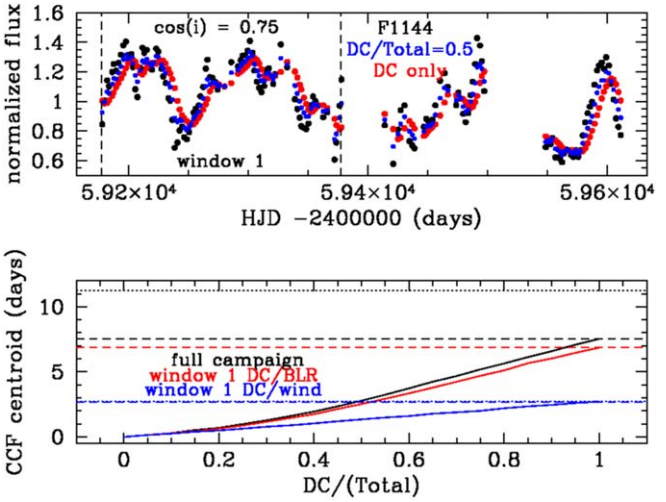

Figure 9. Upper panel: input driving continuum (F1180) for Mrk 817 (black) and output light curves with fractional DC contributions DC/(disk+DC) = 0.5 (blue) and DC only (red). Each light curve has been normalized to its mean value to aid clarity. The location of window 1 (HJD = 2459177–2459377) is indicated by the vertical dashed lines. Lower panel: the measured delay (ICCF centroid) as a function of the DC fractional contribution to the total light for the full light curve (black) and window 1 (red). Also shown is the measured delay for the wind component against its fractional contribution to the total light (blue) without any DC contribution from the BLR. The horizontal dashed lines indicate the measured delay of the DC component only for the full campaign (black; ≈7.5 days), for window 1 (red; ≈6.9 days), and for window 1 for the wind component only (blue; ≈2.7 days). The horizontal dotted lines indicate the MERs for Models 2 and 3 (black; 11.3 days) and for Model 1 (blue; 2.75 days).

We next investigate the delay between the proxy driver and the sum of the driver + DC-band light curve, where the fractional contribution of the DC-band light curve to the total light varies from 0 to 1. Example light curves for the driving continuum—F(1144 Å); black points—and driver+DC with DC fractional contributions to the total light—DC/total = 0.5 (blue) and DC only (red)—normalized to their mean values, for the full campaign, are illustrated in the upper panel of Figure 9. Note that as the DC contribution increases, the variability timescale increases and the variability amplitude decreases as expected. In the lower panel of Figure 9, we illustrate the delay dependence on the DC fractional contribution to the total light for both the full campaign (black) and window 1 (red). Once again, the measured delay increases as the DC contribution to the total light increases.

We have also investigated the same scenario for our Model 1 (small BLR or a DW), where the inner and outer boundaries are much closer to the BH, $\log R({\rm cm}) = 15.75 - 16$. The response function for this case is shown in Figure 8 and as a blue line in Figure 9. The situation here is more similar to the thin-ring case. The measured delay increases with increasing fractional contribution in an approximately linear manner. The mean reduction in lag relative to the measured MER (≈2.6 days) is only about 10%, a consequence of the small MER relative to $T_{\rm char}$.

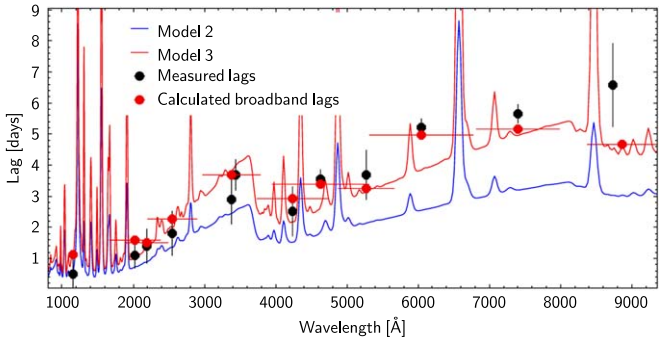

Figure 10. Computed and observed lags for the entire campaign. Data are from C23 and L24, assuming a lag of 0.6 days between the HST/1144 Å and SWIFT/UVW2 bands. An additional lag of 0.5 days is added to all bands to allow for the lag between the ionizing continuum and the HST/1144 Å band (see the text for details). The horizontal red lines show $1/e$ wavelength limits on the SWIFT and ground-based bands. The BLR models are identical to the ones shown in similar colors in Figures 3, 5, and 6.

4.3. General Recommendations

To summarize, numerical simulations applied to the present Mrk 817 campaign suggest that the approximation given by Equation (1) with $f_{\rm lag} = 1$ overestimates the lag induced by the variable BLR by a geometry-dependent factor. The reasons are the exact nature of the driving continuum, the uncertainties on the TF, and the known discrepancy between the MER of the BLR and the duration and characteristic timescale of the variable ionizing continuum. A first-order correction for Models 2 and 3 would be multiplying $\tau_{\lambda,\rm dif}$ in Equation (1) by a factor $f_{\rm lag} \approx 0.5$. For Model 1, with the much smaller BLR, we find a factor $f_{\rm lag}$ of about 0.9. As for other AGNs, modeling a specific BLR using measured line and DC lags could enable better calculations of the TF and lead to improved estimates of this factor. In the following sections, we use $f_{\rm lag} = 0.5$ for Models 2 and 3 and $f_{\rm lag} = 0.9$ for Model 1.

5. Results and Discussion

5.1. Long-term BLR Size and Continuum Lags

Having discussed the uncertainties on the two terms in Equation (1), we can now compare Models 2 and 3 with the measured HST/SWIFT time lags. At this stage, we focus on the mean observed properties and do not consider the luminosity variations discussed in Section 5.2. The data we compare are the lags computed by C23 using the ICCF method (C23, Table 2) and those derived by L24 using the frequency-resolved method (L24, Table 1). The latter were obtained over a frequency range of 0.01–0.02 days^{-1}. The two sets of lags are identical within the errors, and we use their average values in the following discussion.

As explained earlier, we chose the 1144 Å rest-wavelength continuum as our shortest wavelength point and added 0.6 days to all lags calculated relative to the SWIFT/UVW2 band. In addition, we considered the expected lag between the 1144 Å band and the ionizing continuum. This is illustrated in Figure 3, which shows that the combination of broad line wings, weak emission lines, the Rayleigh wings of the Ly-α line, and residual Balmer continuum emission result in total diffuse emission of roughly 10% of the incident continuum radiation. This translates to an additional lag relative to the ionizing continuum of about 0.5 days. Since we do not have direct observations of the ionizing continuum, we added this theoretically derived lag to the measured lags in C23 and L24.

Table 2
Luminosity-dependent MER (Light Days)

Model	2[a]	2a[b]	Ratio
Hβ core	29.0	21.6	1.34
Hβ 4000 km s^{-1}	13.7	10.9	1.26
Hβ total	24.1	18.6	1.30
C IV core	24.6	19.0	1.29
C IV 4000 km s^{-1}	10.5	10.0	1.05
C IV total	18.8	15.1	1.26
He II total	11.0	10.1	1.09
DC	11.2	10.0	1.12

Notes.
[a] $\log R(\rm cm) = 16 - 17.25$.
[b] $\log R(\rm cm) = 16 - 17.10$.

Figure 10 shows a comparison between the model and observations. The best agreement is with Model 3, with a BLR that extends from $\log R(\rm cm) = 16.25$ to $\log R(\rm cm) = 17.5$ (6.9–122 light days). The biggest difference between the model and observations is the z-band lag. As we show in the DW sections below, at least part of it can be explained by even longer lags due to the dust in the torus (see H. Netzer 2022, Figure 2). The predicted and observed line lags listed in Table 1 prefer Model 2 over Model 3, but final measurements of the Hβ lags are not yet available and the C IV lags are changing dramatically over time (Y. Homayouni et al. 2023). Given all the above, Model 3 is our preferred BLR model.

5.2. Luminosity-dependent Lags

Mrk 817 is characterized by large luminosity variations over relatively short periods. This must lead to model-dependent lag variations during the campaign. The measured lags during high and low periods depend on luminosity, the disk SED, and the nature of the driving light curve. Detailed modeling requires information about the time-dependent ionizing SED, which is not available, except for partial information through the analysis of the X-ray observations. The observed change of color ("bluer when brighter") possibly indicates changing accretion rates, but the timescale is very short compared to the viscosity time of thin accretion disks. Given this complexity, we experimented only with a simple scenario, where $L_{\rm bol}$ changes by a factor of 2 (the largest variation observed in the 1144 Å continuum light curve) without a change in the shape of the SED.

Model 2a represents the same BLR assumed earlier exposed to an incident continuum with the same SED as in Model 2 but with $L_{\rm bol}$, which is a factor of 2 smaller. Assuming $R_{\rm in}$ does not change, and an outer boundary that is determined by the sublimation of graphite grains, $R_{\rm out} \propto L_{\rm bol}^{1/2}$. Thus, $R_{\rm out}$(Model 2) $= \sqrt{2} \times R_{\rm out}$(Model 2a). We also include a small variation (2.5%) to the covering factor, which is slightly smaller in Model 2a because of the smaller $R_{\rm out}$.

Table 2 compares the line and continuum lags in Models 2 and 2a. None of the emission-line lags follow the predicted $\sqrt{2}$ reduction in the time lag. Lines more efficiently emitted in the outer BLR, like Hβ, are closer to this prediction. Other lines, like He II λ1640, are coming from the innermost BLR and their MER hardly changes, despite the large change in line luminosity. This is also the case with the DC emission. These

tendencies are even clearer when examining lag variations in different parts of the line profiles (not shown here). The lags of the line cores emitted by the outer BLR change the most, while the far wings, 4000 km s^{-1} from the line center, are emitted much closer to the ionizing source, where the structure of the line-emitting zone hardly changes.

We have also examined a similar situation for Model 3 by defining Model 3a, where $L_{\rm bol}$ is reduced by a factor 2 and the outer radius is changed from $\log R({\rm cm}) = 17.5$ to $\log R({\rm cm}) = 17.35$. The relative decreases in the various MERs are similar to those found when comparing Model 2 to Model 2a (see Table 2).

Finally, we have experimented with a model with smaller $R_{\rm in}$. Such a case results in larger changes in line and DC lags. However, there is no simple mechanism to justify such an assumption, except perhaps the possibility that small-optical-depth clouds may become optically thick during lower-luminosity phases.

5.3. DWs and BLR Obscuration

M. Dehghanian et al. (2020) discussed the idea of a DW in an attempt to explain the 2014 HST observations of NGC 5548 (the AGN STORM 1 campaign). In this case, the normally correlated UV continuum and broad emission-line variations decoupled (M. R. Goad et al. 2016; L. Pei et al. 2017). The wind was suggested to rise almost perpendicular to the disk's surface, on the line connecting the ionizing source to the BLR, and its base was assumed to be optically thick to some but not all of the ionizing radiation. This changes considerably the level of ionization and the emergent BLR spectrum. It also contributed broad, high-velocity components to the high-ionization lines. As the wind rises from the disk's surface, part of it becomes observable through X-ray and UV broad absorption features. The wind becomes more tenuous with time, diminishing absorption features over several weeks.

A similar spectral behavior was observed in Mrk 817 and has been discussed in previous papers in this series. Two scenarios have been proposed to explain the observed changes in the overall geometry of the source, one based on the changing lags of the C IV line and one on the changing continuum lags. Y. Homayouni et al. (2024) divided the first 201 days of the campaign into three temporal windows, spanning 50, 55, and 96 days. They then correlated the 1144 Å continuum with the C IV line and discovered very different lags of 11.7, 1.9, and 3.9 days, respectively. They proposed a diminishing obscuration of the BLR by a shielding DW, which resulted in a considerable shortening of the lag of the C IV line. There is clear evidence, from UV and X-ray observations, for the presence of wind along our line of sight to the source in the first part of this period. The analysis was carried out on the total line flux and did not consider the substantial lag differences between the line core and its red wing found in Y. Homayouni et al. (2023).

L24 investigated a scenario of a DW that changes its direction and column density over 420 days, starting from the beginning of the campaign. According to L24, this resulted in large observed differences in continuum lags between Epoch 1 (HJD = 2459177–2459317) that overlap with temporal windows 1 and 2 and part of temporal window 3, Epoch 2 (HJD = 2459317–2459457), and Epoch 3 (HJD = 2459457–2459597). Possible geometrical configurations leading to the two scenarios are illustrated schematically in Y. Homayouni et al. (2024) and L24.

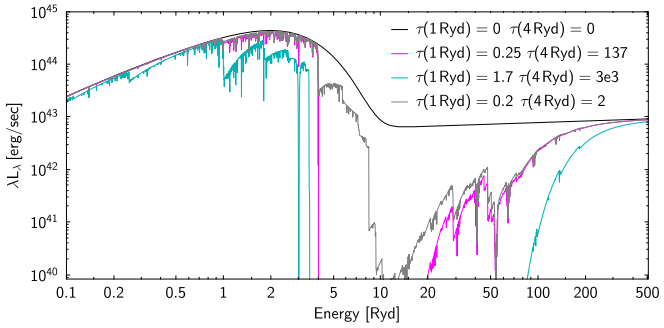

Figure 11. Various absorbed SEDs characterized by their optical depths at 1 and 4 Ryd.

Table 3
Fractional Transmitted Luminosity

SED	τ(1 Ryd)	τ(4 Ryd)	1–100 Ryd	4–100 Ryd
1 (black)	0	0	1.0	0.146[a]
2 (gray)	0.2	2.0	0.769	0.029
3 (magenta)	0.25	137	0.744	$<10^{-3}$
4 (cyan)	1.7	$>10^3$	0.335	$<10^{-3}$

Note.
[a] L(1–100 Ryd) = 6.23×10^{44} erg s^{-1}.

The idea of an obscuring DW during the first 140 days of the campaign is not without difficulties. A detailed look into the C IV line behavior (Figure 8 of Y. Homayouni et al. 2023) shows that the longest measured lags are associated mostly with the line core and the shortest ones with the high-velocity line wings, as expected from a gravitationally bound system of clouds. Given the unusual driving light curve of Mrk 817 discussed in Section 4 and the short durations of the three temporal windows, the impression of large changes in the lag of the entire line may be due to different ways of combining the core and the wings of the line, rather than a large-column-density wind that obscures the BLR from the ionizing radiation. Moreover, such a DW during Epoch 1 would result in intense DC emission and considerably shorter continuum lags, unless a very special geometry is assumed. Such shortening is not observed.

5.4. Specific DWs

Below, we investigate four generic DW scenarios. The properties of the winds are defined by their location, column density, covering factor, and optical depth as a function of time. The scenarios are distinguished by the flux transmitted through the wind material and are illustrated in Figure 11 and Table 3. We explored a range of wind locations between 2 and 4 light days from the BH. The conclusions about the line and continuum luminosities for shielded BLRs depend only weakly on this choice. Still, the line velocity and variability from the gas in the wind depend on this assumption. The four scenarios are:

1. All ionizing luminosity is absorbed by a high-column-density wind (not shown in Figure 11). In this case, the wind can be considered a collection of RPC BLR clouds similar to the ones assumed in Model 1, but probably at a shorter distance from the central BH.
2. In this case, represented by a gray line, the fraction of the 4–100 Ryd radiation absorbed by the wind is relatively large, and the absorbed fraction of the 1–4 Ryd continuum

is negligible. For equatorial winds of this type, the effect of obscuration is minor spectral variations in several strong UV emission lines, but no DC emission variations.

3. The wind absorbs all the 4–100 Ryd flux (the magenta line in Figure 11), but only a small fraction of the 1–4 Ryd flux. The total reduction in the 1–100 Ryd flux is small, of order 25%. For shielded BLR gas, small changes in high-ionization lines are expected.
4. The wind absorbs all the 4–100 Ryd flux and ≈50% of the 1–4 Ryd flux (the cyan line in Figure 11). For shielded BLR gas, significant variations in line and DC emissions are expected. This case is the one most similar to the "equatorial obscurer" investigated by M. Dehghanian et al. (2020).

5.4.1. Case (i): RPC DWs

Our Model 1, shown in green in all previous figures, represents a small-sized BLR, but could also be used to study the properties of a DW with similar size and location. An outflow of such "RPC Wind" will affect the total observed line and continuum luminosities and their lags during parts of the campaign. The assumed geometrical covering factor of the wind is 0.2–0.3. In the example shown so far (Model 1), $\log R(\mathrm{cm}) = 15.75 - 16$, but smaller distances have also been considered (see Appendix A). As in all RPC models, the gas density is determined by the local radiation pressure of the central source. Close to the ionization front inside typical clumps, this is $10^{12.4-12.9}\,\mathrm{cm}^{-3}$.

The direction of the wind's motion and its density and column density change over time. Far from the disk, the gas is so dilute that its emission is practically unobserved. We assume that close to the launch locations, the direction is perpendicular to the disk's surface, and the velocity is close to the escape velocity at this location. Given the chosen inclination of the BLR disk (41.°4), we can calculate the observed wind velocity. The gas in the wind can block the ionizing radiation from reaching the entire BLR, part of the BLR, or no part at all. For the latter case, the total emission from the system (DC+lines) will be enhanced.

The column density of the clumps in the wind is an important consideration. For all models discussed so far, it was assumed to be $10^{23.5}\,\mathrm{cm}^{-2}$. At a distance of 10^{16} cm or larger, this is consistent with gravitationally bound clouds. At smaller distances, the column density of the ionized gas is larger (at the back of the cloud, $n_e \approx n_{\mathrm{H\,I}}$), and a sizable fraction of the ionization radiation can escape from the far side of the clouds. We have therefore experimented with thicker clouds with a column density of $10^{24}\,\mathrm{cm}^{-2}$ and show several examples in Appendix C.

The lag of the DC radiation emitted by the gas in the case (i) wind is much smaller than the lag of the BLR gas, primarily because of the much closer location of this component (Figure 5). The high-ionization lines like C IV are predicted to be very broad compared with their FWHM in the BLR, and the lags of the very broad wings are very short. Such winds produce very weak Balmer lines.

Given this, we suggest that an ejection of a DW with the properties assumed here (Model 1) could occur close to the end of Epoch 1, provided the wind is rising rapidly and changes its 1–4 Ryd optical depth over a time that is short compared with 140 days (the duration of Epoch 1 and Epoch 2). In fact, following the observed Lyman and Balmer lines and the core of C IV during Epoch 1 and Epoch 2, we could not identify any period where the line intensities are reduced by large factors, as expected for complete shielding of the BLR. Later, the optical depth of the rising wind decreases, making it more similar to the other types of winds discussed here. As explained below, a Case (iv) wind best fits the conditions observed in Epoch 2.

The wind ejection process described here is likely to happen continuously during most of the AGN STORM 2 campaign. Thus, the line-of-sight X-ray-absorbing gas observed in Epoch 1 can be the remnants of an ejection event before the beginning of Epoch 1, and the DW observed during Epoch 2 can lead to the next epoch of X-ray-absorbing gas between HJD = 2459530 and 2459600 (see E. R. Partington et al. 2023).

Finally, a comment about X-ray illumination and the location of a high-column-density DW. The self-gravity radius of a standard thin disk, consistent with the mass and accretion rate measured for Mrk 817, is about $1000R_{\mathrm{g}}$. This is also the estimated launch location of the wind, based on measured continuum lags, and perhaps also the high-velocity wings of Ly-α and C IV. The DW in question is a barrier between the central X-ray source and the extended disk, and it is hard to imagine X-ray-heated parts 5 or 6 light days from the BH unless the corona extends to extreme heights above the disk surface. Thus, high-column-density DWs and X-ray-illuminated regions at large distances seem inconsistent.

5.4.2. Cases (ii) and (iii): X-Ray Winds and Small-optical-depth Equatorial Winds

Cases (ii) and (iii) are characterized by medium to very high τ(4 Ryd) and small τ(1 Ryd). We investigated their contributions to the Mrk 817 observations assuming two locations: close to the disk's surface inside the BLR ("equatorial wind") and along the line of sight to the source ("X-ray wind"). We provide detailed calculations for case (iii) and discuss, in more general terms, various types of X-ray winds.

We calculated a combined wind–BLR model made up of two components: an equatorial DW, illuminated by the bare high-luminosity SED considered earlier, and a BLR identical in its geometrical properties to Model 2 ($\log R(\mathrm{cm}) = 16 - 17.25$), illuminated by the continuum transmitted through the wind. We compared this model to the unshielded Model 2 discussed earlier.

Figure 12 compares the global spectra of the case (iii) wind, the shielded BLR, and the unshielded BLR. Clearly, for this wind, the broad wings of lines from ions of very-high-ionization potential, like He II λ1640, are produced mostly by the wind and lines with lower-ionization energy, including C IV, have contributions from both components. The emission of hydrogen Lyman and Balmer lines is dominated by the obscured BLR, where conditions for the production of these lines are more favorable. The DC emission is almost entirely from the shielded BLR.

Strong X-ray absorption features were observed over the entire Mrk 817 campaign. The NICER observations discussed in E. R. Partington et al. (2023) provide estimates of the column density, line-of-sight covering factor, and ionization parameter of this gas. The ionization parameter is based on constant-density photoionization models. The similar velocities of the broad C IV and Si IV absorption lines with X-ray absorption lines (F. Zaidouni et al. 2024) during one epoch, combined with the assumption that such velocities are of the order of the projected escape velocity, provide a rough estimate of the location of the gas at around 10^{16} cm. The observed spectrum is made of two independent components, one marginally optically thick (X-ray wind) and one with a very large optical depth (the BLR), at very different distances.

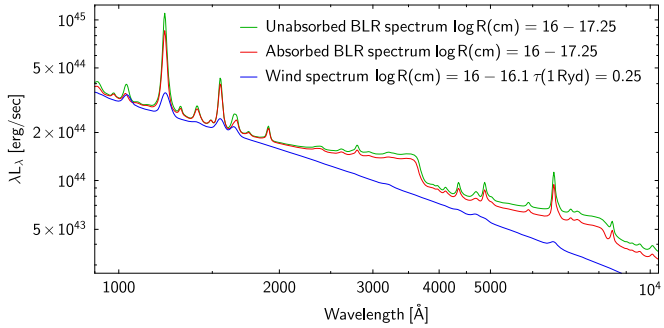

Figure 12. Absorbed (red), unabsorbed (green), and case (iii) wind (blue) spectra showing the significant contribution of the wind to the strong UV lines and an insignificant contribution to the DC emission.

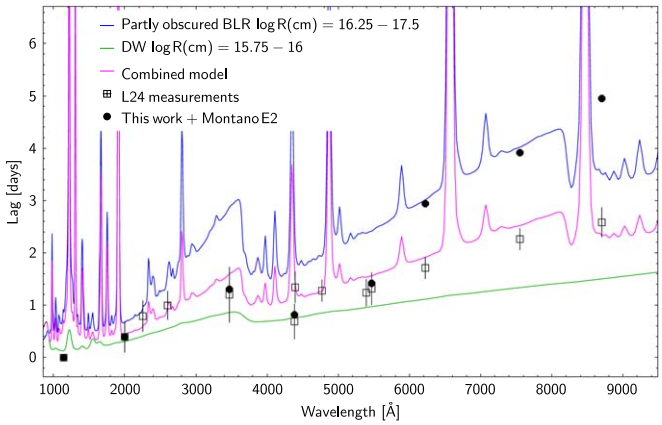

Figure 13. The computed lags of a partly transparent DW (in green), a partly shielded BLR (in blue), and their emissivity-weighted combination (in magenta). The properties of the various components are marked in the figure. The models are compared with two ways of measuring lags in Epoch 2: frequency-resolved lags (L24) and ICCF–PyCCF lags (this work and J. Montano 2024). Note the sharp rise of the *r*-, *i*-, and *z*-band PyCCF-measured lags, which we interpret as due to the torus dust component (see the text for further explanation).

We calculated the expected emission from clouds with properties similar to the mean properties observed by E. R. Partington et al. (2023) during Epoch 1: a column density of $10^{23}\,\mathrm{cm}^{-2}$ and an ionization parameter of $\xi = L(1-1000\,\mathrm{Ryd})/nR^2 \approx 1$. We assumed that the X-ray wind extends from 10^{16} to $10^{16.1}$ cm (the exact range is not critical, since the ionization parameter was assumed to be the same in all clouds). While the global covering factor during Epoch 1 is unknown, we can use the changing column density and line-of-sight covering factors listed in E. R. Partington et al. (2023) to estimate a mean (over time) global covering factor of 0.2–0.4.

The calculated joint spectrum (not shown here) is similar to the combined spectra shown in Figure 12. In particular, an X-ray wind with the mean properties observed in Epoch 1 contributes very little to the total DC emission observed during our campaign.

We also compared our X-ray absorber model with an RPC model at the same mean distance and density at the illuminated face, identical to the density in the constant-density model. The critical issue is the total optical depth, which needs to be very large to justify the RPC assumption. We found that some of the clouds, those with a column density exceeding $10^{23.2}$ cm^{-2}, with small ionization parameters, are indeed pressure-confined. Thus, some of the constant-density clouds with the properties listed in E. R. Partington et al. (2023) are inconsistent with the main assumption made in the present paper. We did not attempt to calculate all these models in detail.

Given this comparison, the X-ray-absorbing gas observed in Epoch 1 cannot significantly affect the observed continuum lags because of its weak DC emission. On the other hand, a fraction of the observed line flux during this epoch, and perhaps during different times, can be attributed to such gas.

5.4.3. Case (iv): Intermediate-optical-depth Equatorial Winds

This case is the most similar to the NGC 5548 model proposed by M. Dehghanian et al. (2020). The 1 Ryd and 4 Ryd optical depths (see Table 3 and the cyan curve in Figure 11) are such that about half of the 1–4 Ryd ionizing continuum is absorbed by the wind. Our wind calculations extend over the range $10^{15.75}$–10^{16} cm and assume a column density of $10^{22.8}$ cm^{-2} for individual clumps. They confirm that this column density is large enough to produce significant DC emissions from the wind and to dominate the high-velocity wings of lines like Ly-α and C IV. The BLR is exposed to the partly shielded ionizing flux. The high-ionization lines are much weaker than in the case of no shielding, and the DC is strong but not as strong as the DC luminosity of the wind.

Figure 13 shows three computed curves of wavelength-dependent lags: one from the shielding wind (green line), one from the partly obscured BLR (blue line), and the emissivity-weighted lags for a combination of these two cases (magenta line). Continuum RM measurements could easily detect the lag differences between a pure BLR—for example, Model 3, shown in Figure 10—and a wind–BLR combination like the one shown here.

Figure 13 also shows broadband lags measured in two different ways during Epoch 2: frequency-resolved lags from L24 computed for the 20–70 days^{-1} frequency range and ICCF and PyCCF lags calculated by us and by J. Montano et al. (2024, in preparation). The two sets of lags differ substantially at the longest-wavelength bands, suggesting that the *r*, *i*, and *z* bands are affected by an emission and/or reflection component at a distance of 70 or more light days. As argued below, at least part of the difference can be explained by dust emission from the nuclear torus in Mrk 817.

To summarize, the signature of a shielding DW, which absorbs most of the ionizing radiation, is equivalent to that of a small optically thick BLR at a very small distance from the BH, similar to our Model 1. This may result in a short transitory phase during which the more distant BLR responds to the continuum flux emitted before the wind is launched. Later, the line and continuum emission from the obscured BLR declines dramatically, and most of the observed emission is from the rising wind. There is no indication that this has happened during the AGN STORM 2 campaign, because all Balmer lines and other strong emission lines do not show such behavior.

A rising large-optical-depth wind changes its properties and becomes similar, for some time, to what is defined here as a case (iv) wind. Such a phase could last 100–200 days and perhaps even longer. During this time, the observed emission lines and DC emission are contributed from both components: the rising wind and the partly shielded BLR. As shown in Figure 13, the calculated continuum lags fit well the lags observed during Epoch 2, provided the faraway dusty torus contribution is insignificant.

The case (ii) and (iii) winds—those winds with large τ (4 Ryd) and small τ(1 Ryd)—represent well the X-ray-absorbing winds observed in Mrk 817. Such winds result in minor

variations of the spectrum of the shielded BLR. In particular, the combined wind-shielded BLR model is similar in spectral shape to the case of unshielded BLR, except that the wings of the high-ionization lines originating in the wind component are broader and have shorter time lags. There is no significant DC emission by such DWs.

Our wind scenarios are meant to be general and do not follow all possible time-dependent geometries. They are based on the 1 and 4 Ryd optical depths and not on a systematic coverage of the density, column density, and ionizing flux parameter space, as in M. Dehghanian et al. (2020). Being sensitive to the changing optical depth suggests that the properties of all those winds will change considerably during the "high-L" and "low-L" episodes described earlier.

5.5. The Dusty Torus and Long-wavelength Lags

None of the models considered so far include thermal dust emission by a torus-like structure beyond the sublimation radius of graphite grains. Such structures are very common in high- and low-luminosity AGNs, and their properties have been discussed in numerous publications (e.g., H. Netzer 2015 and references therein). In particular, near-infrared (NIR) monitoring of many sources (e.g., S. Koshida et al. 2014; GRAVITY Collaboration et al. 2020) show that the K-band NIR flux lags the V-band continuum with a delay that is roughly three to four times the typical delay of the Hβ line. The observed K-band flux in Mrk 817 suggests a similar torus with a delay of its innermost illuminated face, made of pure graphite grains, of about 80 days. Given that much of the K-band flux is due to graphite grains with temperatures exceeding about 1500 K (the sublimation temperature of silicate ISM grains), we should consider the effect of this emission on the i and z bands of the source as well as the additional delay relative to the optical–UV flux. This issue has been discussed in several earlier publications, such as S. F. Hönig (2014), K. T. Korista & M. R. Goad (2019), and H. Netzer (2022).

A detailed investigation of the dust-induced variations in Mrk 817 is beyond the scope of the present paper. Such an investigation should consider various torus geometries, a range of dust temperatures, and, most importantly, the nature of the optical–UV driving light curve. Here, we only demonstrate the potential additional complexity due to this process.

We consider the case (iv) wind discussed earlier and the lag curves shown in Figure 13. We also assume that for Mrk 817, $\lambda L_\lambda(2\ \mu\mathrm{m}) = 8.6 \times 10^{43}$ erg s^{-1} (a forthcoming AGN STORM 2 paper). We further consider several BBs with $T = 1500$–1700 K and their contributions to the observed spectrum. The case illustrated below assumes $T(\mathrm{dust}) = 1600$ K.

There are various ways to add the dust-induced lag to the illuminated disk and DC-induced lags. The DC luminosity in our case (iv) wind is comparable to the accretion-disk luminosity in the i and z bands. Given this, we changed the definition of L_{tot} used earlier to be $L_{\mathrm{tot}} = L_{\mathrm{diff}} + L_{\mathrm{inc}} + L_{\mathrm{dust}}$ and added a new term, $\tau_{\lambda,\mathrm{dust}}$, defined as

$$\tau_{\lambda,\mathrm{dust}} = 80 f_{\mathrm{lag}} \times \frac{L_{\mathrm{dust}}}{L_{\mathrm{tot}}}\ \mathrm{days}\ , \qquad (2)$$

to Equation (1). Here, 80 days is the assumed K-band delay based on the mean measured Hβ delay and $f_{\mathrm{lag}} = 0.5$, as used in all BLR models. The results are shown by a black curve in Figure 14. This approximation shows how significant dust delays can be at long wavelengths.

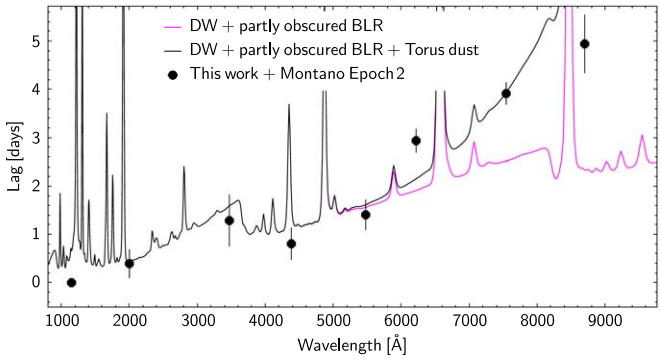

Figure 14. The DW BLR model from Figure 13 combined with torus dust, assuming $T(\mathrm{dust}) = 1600$ K.

Our simplified estimate was not tested by numerical simulations. Therefore, the value of f_{lag} is only a guess, and the procedure for combining three variable components (disk, diffuse emission, and dust) needs to be confirmed. Moreover, the Epoch 2 period is only 140 days long—very short, considering the ≈80 day delay signature for the hot dust. Figure 18 in Appendix D illustrates this issue. A more likely possibility, which we cannot yet confirm, is a steady rise or fall of L_{dust} during this period. Nevertheless, dust delays cannot be excluded and should be more thoroughly investigated.

5.6. Complications and Uncertainties

The models presented here focus on broadband continuum lags with uncertainties typical of this type of measurement. They are not meant to provide a complete fit of the response and lags of all emission lines. This would require a more careful analysis of the changes in time and amplitude of the driving light curve with the location and velocity-dependent response of the BLR gas.

Reproducing the observed interband continuum delays depends on various assumptions and uncertainties. Depending on redshift, all the SWIFT and ground-based bands include one or more broad and variable emission lines. The MERs of many lines differ from the MER of the DC emission, which is the primary factor affecting the observed lags. An important example is the C III]λ1909 emission line (see Figure 10 of this paper and Figure 13 in C23), which contaminates the SWIFT/UVW2 band. According to our Models 2 and 3, the MER of this line is about 2–2.5 larger than the MER of the DC emission. This can increase the lag in this band by 10%–30%.

A related issue is the computed intensity of the hydrogen Balmer lines, the strong UV and optical Fe II lines, and the Mg II doublet at 2800 Å. As discussed in earlier publications, most recently in H. Netzer (2020, 2022), present BLR models tend to underestimate the intensities and equivalent widths of these lines. The too-weak computed UV Fe II lines are evident in Figure 4. The bands most affected by this are the three SWIFT/UVOT bands and optical bands, which overlap with the strong Hα and Hβ lines. This tends to increase the observed lags compared with the model predictions.

An uncertainty of a different type is the radial dependence of the covering factor, $C(R)$. The power-law dependence assumed here is common to several published BLR models. Its primary justification is the good agreement between modeled and observed line lags. The simple approximation we used, $dC(R) \propto R^{-\beta} dR$, with $\beta = 2$, is typical of successful BLR models, but somewhat different values of β are just as good.

Additional possibilities not considered here are nonradial distributions of optically thick and optically thin clouds.

The assumed total covering factor of the clouds used in the simulations (0.2) is likely smaller than the global geometrical covering factor of the flared-disk BLR. This would result in a somewhat different TF but is unlikely to be a significant source of uncertainty. Another uncertainty that depends on the BLR geometry and the characteristics of the driving continuum is the exact value of $f_{\rm lag}$(TF). A factor not included in the present calculations is the anisotropy of the optically thick line emission, particularly the Balmer lines.

Several other assumptions, such as the microturbulent velocity inside the cloud and the gas metallicity, were not discussed in detail. H. Netzer (2020) discussed these in the general framework of the RPC model and showed them to be of secondary importance if the microturbulent velocity does not exceed about 30 km s^{-1}.

Finally, as Figure 2 shows, the disk SED in Mrk 817 is changing with luminosity in a way that affects the ionizing SED, the global level of ionization of the gas, and perhaps also the outer boundary of the BLR. The present paper considers only a changing luminosity not associated with a change in SED shape. More advanced accretion-disk models are required to test other possibilities.

6. Conclusions

We have combined information from several papers in the AGN STORM 2 series about emission-line lags, X-ray and UV absorption features, and continuum lags with new BLR and DW models to present a comprehensive view of the nucleus of Mrk 817. Our main findings can be summarized as follows:

1. DC emission, with additional contributions from strong and broad emission lines, can explain the broadband continuum lags observed in this source. In all cases considered here, the X-ray-illuminated accretion disk contributes only a small fraction of the observed continuum lags, and there is no need to assume disk sizes exceeding the size of a standard thin accretion disk.
2. Our BLR models cover different possible geometries and a large range of distances from 2 to 122 light days. Modeling these assemblies of RPC clouds using the SED observed during the first 100 days of the campaign, we can explain the observed lags of Hβ, C IV, and several other emission lines. COS-STIS spectra of the source during high and low flux levels indicate that the SED is bluer when brighter. Computed models that assume luminosity variation but no change of SED shape are also consistent with the measured emission-line and DC time lags.
3. We suggest a modified procedure based on older methods and a new multiplication factor, $f_{\rm lag}$(TF), for combining DC lags with the lags predicted by simple, X-ray-illuminated, thin accretion disks. We present extensive numerical simulations showing that $f_{\rm lag}({\rm TF}) \approx 0.5$ for typical BLR configurations. In more general situations, including a combination of DW and BLR, this factor depends on the specific TF and the nature of the driving continuum light curve. We suggest that continuum light curves shorter than about 100 days may bias the measured lag in a way that questions the derived BLR geometry.
4. We suggest that case (iv) winds—those with $\tau(1\,{\rm Ryd}) \approx 2$—were common in Mrk 817 during the AGN STORM 2 campaign. In particular, we show that the significant shortening of the continuum lags during the period HJD = 2459317–2459457 (Epoch 2) is due to the combination of such a wind with a partly shielded BLR. This may well be a later stage of a larger-column-density wind that was ejected from the disk at an earlier stage, at the end of Epoch 1. The wind does not obscure our line of sight to the source until much later, where its optical depth is further reduced (the case (ii) and case (iii) winds), and X-ray absorption features become evident.
5. BLR obscuration by small $\tau(1\,{\rm Ryd})$ winds leads to noticeable variations of the global observed spectrum, particularly the width and lags of several high-ionization lines like Ly-α, He II, and C IV.
6. The launch locations of high-column-density DWs set upper limits on the distance of the parts of the disk that can be significantly heated by the central X-ray source.

Acknowledgments

This article is part of the series of papers by the AGN STORM 2 collaboration. Our project began with the successful Cycle 28 HST proposal 16196 (B. M. Peterson et al. 2020). Support for Hubble Space Telescope program GO-16196 was provided by NASA through a grant from the Space Telescope Science Institute, which is operated by the Association of Universities for Research in Astronomy, Inc., under NASA contract NAS5-26555. We are grateful to the dedicated Institute staff who worked hard to review and implement this program. We particularly thank the Program Coordinator, W. Januszewski, who made sure the intensive monitoring schedule and coordination with other facilities continued successfully.

D.I., A.B.K, and L.Č.P. acknowledge funding provided by the University of Belgrade Faculty of Mathematics (contract 451-03-66/2024-03/200104) and Astronomical Observatory Belgrade (contract 451-03-66/2024-03/200002), through grants by the Ministry of Education, Science, and Technological Development of the Republic of Serbia. D.I. acknowledges the support of the Alexander von Humboldt Foundation. A.B.K. and L.Č.P. are grateful for the support from the Chinese Academy of Science's President's International Fellowship Initiative (PIFI) for visiting scientists. N.A. acknowledges support from NSF grant AST 2106249 and NASA STScI grants AR-15786, AR-16600, AR-16601, and HST-AR-17556. G.K. and G.D.R acknowledge support from STScI grant GO-16196.

We thank Jonathan Stern for useful discussions about RPC models.

For the purpose of open access, the author has applied a Creative Commons Attribution (CC BY) license to the Author Accepted Manuscript version arising from this submission.

Facility: SWIFT, HST (COS, STIS).

Software: Cloudy (G. J. Ferland et al. 2017).

Appendix A
Various MERs

The exact meaning of the MER used here requires further explanation. For a broad emission line, the total MER is the one usually compared with the lag of the total line luminosity, which is integrated over a large velocity range and, hence, for a

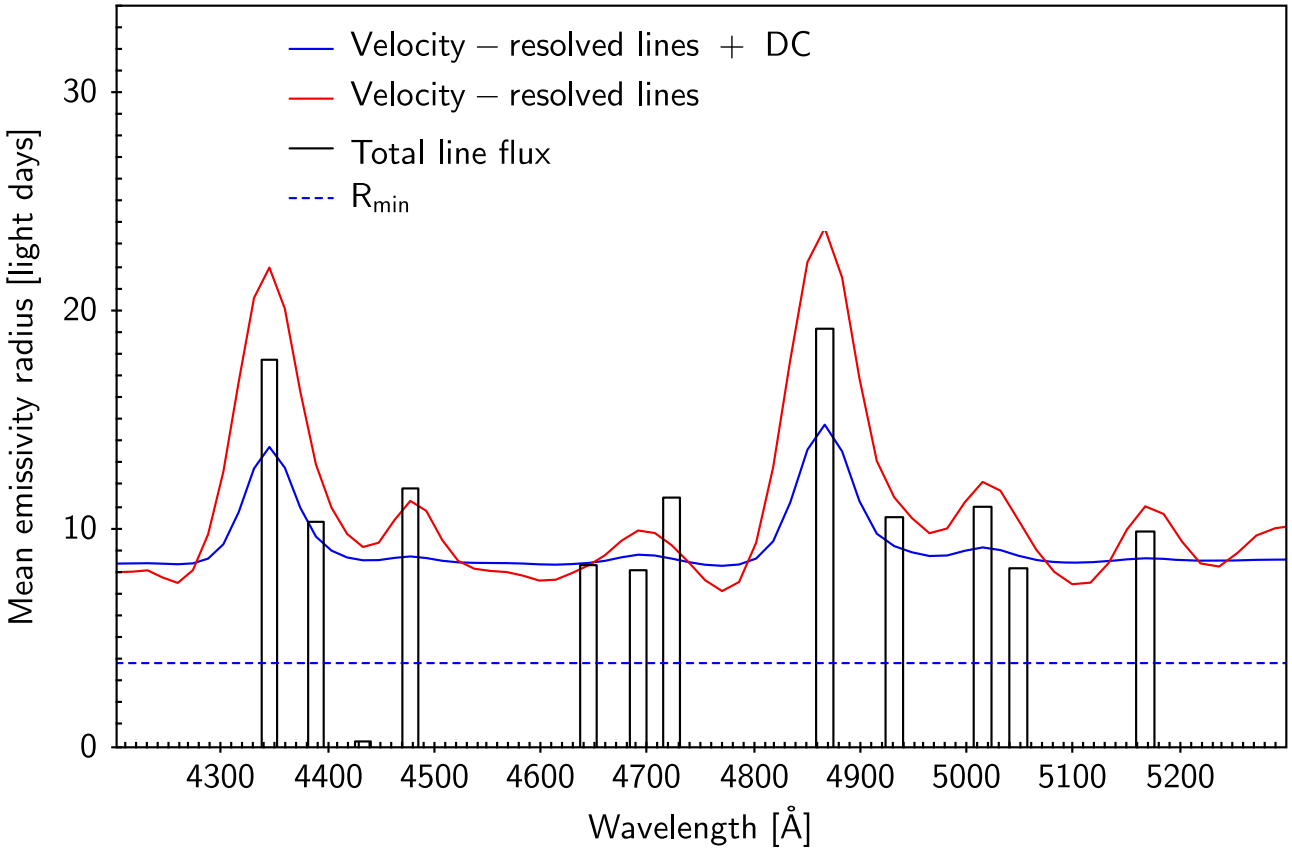

Figure 15. Various types of MERs over the Hγ and Hβ line region. Black: integrated-line-luminosity MER (the quantity normally measured in 1D RM campaigns). Red: velocity-resolved line lags. Blue: broadband MER lags that include DC MERs in line-free regions of the spectrum or combinations of velocity-resolved lines and DC emission closer to the line core. This is normally smaller than the MER of velocity-resolved lines, since the MER of the DC is considerably smaller (≈50%) than the MER of the Balmer lines.

gravitationally bound BLR, a large range of distances. Velocity-resolved RM MERs are smaller than the total MER in the line wings and larger in the line core. A third type of MER is shown in Figure 5. The vertical axis gives a combined line+DC MER at each wavelength, which can differ from the other MERs discussed here. An illustration of the three different MERs in Model 2 for the spectral region containing the Hβ and Hγ lines is shown in Figure 15.

Appendix B
Comparison with Frequency-resolved Lags

E. M. Cackett et al. (2022) and L24 used frequency-resolved methods (e.g., P. Uttley et al. 2014) to separate the total TF (or the impulse-resolved function) into disk and BLR parts:

$$\psi_{\rm tot}(t) = (1 - f_\lambda)\psi_{\rm disk}(t) + f_\lambda\,\psi_{\rm BLR}(t), \qquad \text{(B1)}$$

where f_λ represents the relative contributions of the BLR to the total TF at wavelength λ and hence the physics and the size of the BLR. This approach avoids using various time filters like detrending and Gaussian smoothing. They also suggested representing $\psi_{\rm BLR}$ by a two-parameter log-normal distribution function, where the parameters M and S represent the function's median (e^M) and standard deviation. L24 used the observed Hβ lag to suggest that the first part (Epoch 1) of the campaign, when the obscuring X-ray column was large, can be represented by a log-normal function with $e^M = 24$ and $S = 0.9$ day. Epoch 2, when the X-ray column was much smaller, was described by $e^M = 24$ days and $S = 1.7$ days. Given this choice of parameters, one can solve for f_λ that best fits the observed lags.

Our time-domain forward approach can be compared with the frequency-resolved analysis by comparing the TF of the DC (the dominant factor contributing to the continuum lags) to the Hβ-based log-normal distribution function. This is shown in Figure 16. The two functions are very different, not so much because of their different shapes, but mainly because the MER of the DC is much smaller (≈50%) than the MER of the Hβ line. This would result in very different contributions of the BLR to the total TF (f_λ in Equation (B1)).

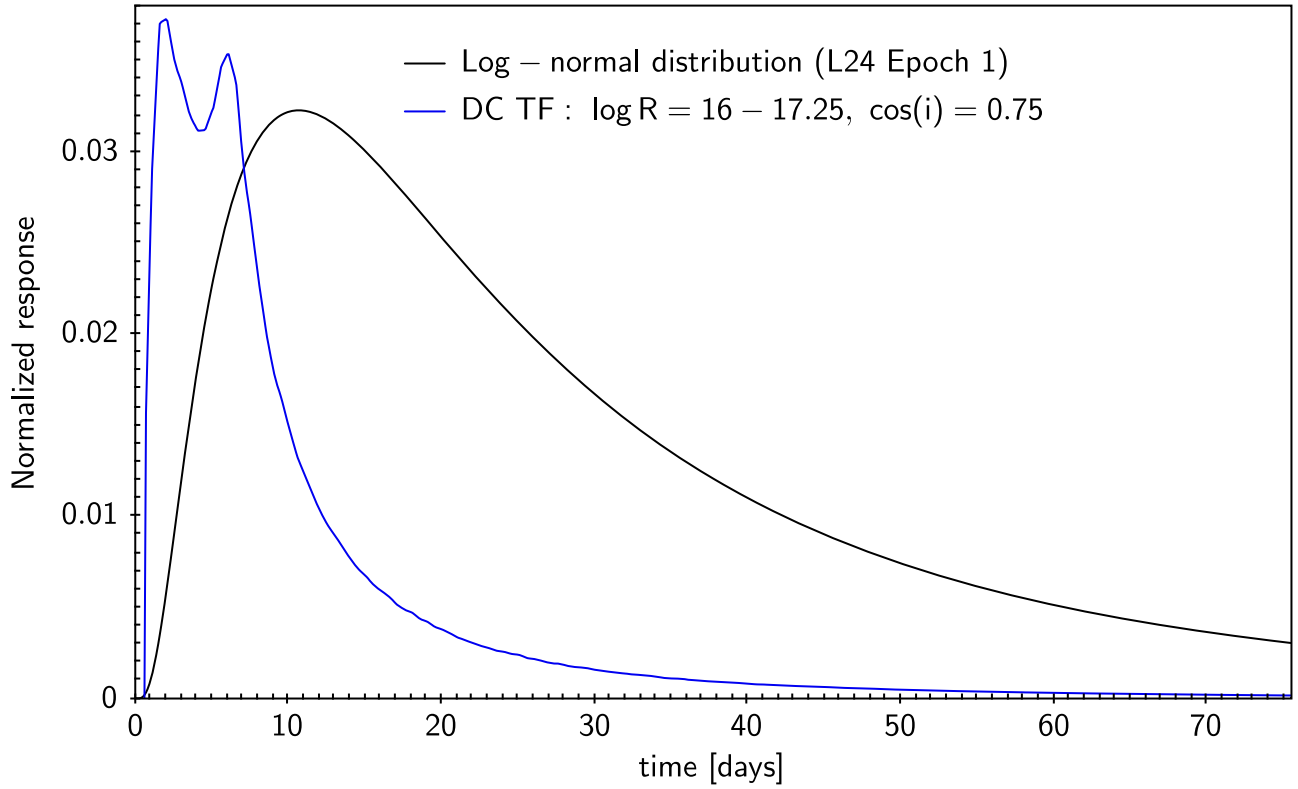

Figure 16. A comparison between the log-normal distribution used in L24 for Epoch 1 and the TF of 7995 Å DC in our Model 2 with $\log R(\mathrm{cm}) = 16 - 17.25$. The MERs are 25 light days for the log-normal distribution and 11.3 light days for the 7995 Å TF.

Appendix C
Additional DW Models

Additional wind models that cover a range of distances equal to or smaller than the range assumed in Model 1, all with a column density of $10^{24}\,\mathrm{cm}^{-2}$, have been computed. In these cases, the luminosity emitted over the Balmer continuum wave band is smaller than the luminosity of the standard case shown in Figure 3, where the column density is $10^{23.5}\,\mathrm{cm}^{-2}$. The main reason is the increased opacity of the gas over this band, which results in more absorption of the incident continuum. This increases the ionization of neutral hydrogen and the locally emitted bound–free emission. However, much of the additional emitted radiation is spread over wavelength bands outside the range shown here.

The computed lags for such winds are shown in Figure 17. Some lags are very short, similar to those predicted for the X-ray-illuminated disk.

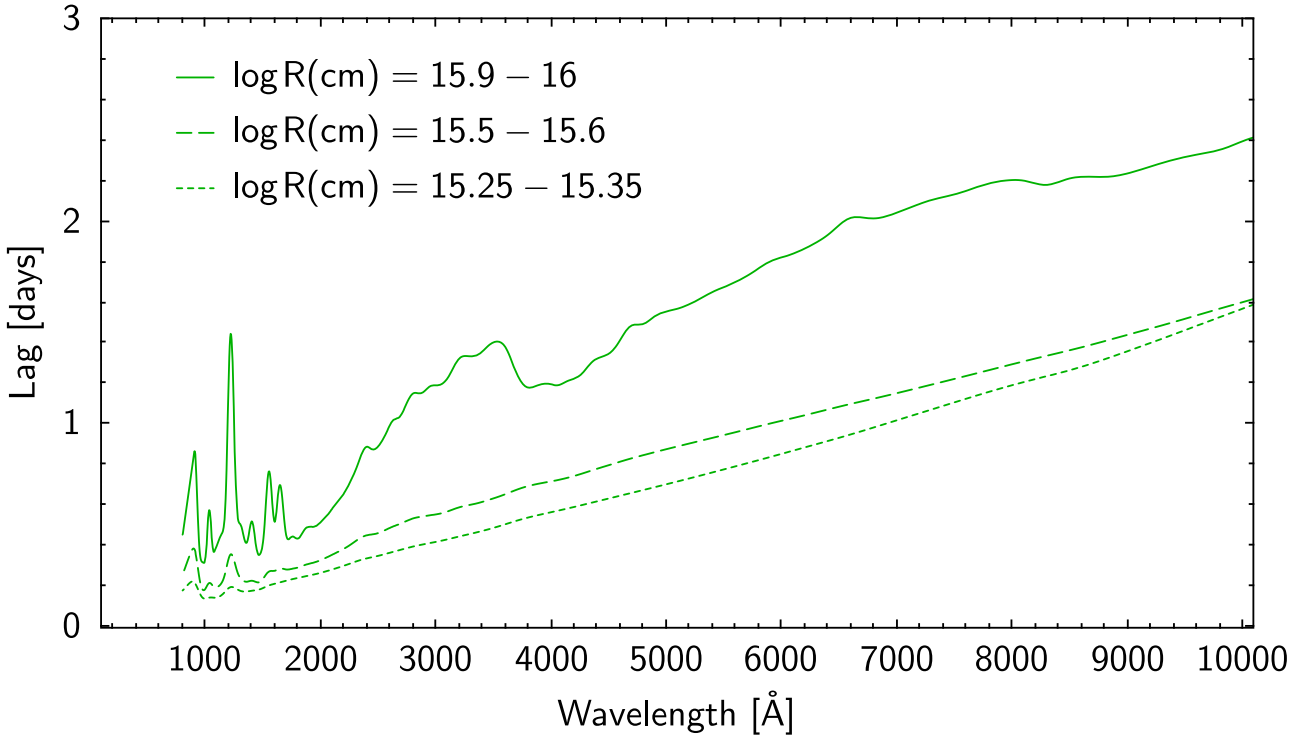

Figure 17. Wavelength-dependent lags for winds with a column density of 10^{24} cm^{-2} and distances as marked.

Appendix D
Delay Dependence on $T_{\rm char}$ and $T_{\rm dur}$

To illustrate the dependence of the measured lag of the DC component on the characteristic timescale of the driving continuum $T_{\rm char}$ and campaign duration $T_{\rm dur}$, we drive our model BLR (Model 2) with simulated light curves generated from a CAR1 process (e.g., B. C. Kelly et al. 2009), sampled at 1 day intervals. We fix the variance of the simulated driving light curve but vary the damping timescale, measuring the lag from the centroid of the ICCF. Figure 18 illustrates the dependence of the measured lag as a function of the damping timescale, with the damping timescale in the range 20–400 days, and campaign durations of length $T_{\rm dur} = 500$, 1000, and 2000 days.

In all cases, the measured delay shows a steep dependence on the damping timescale of the driving continuum for small $T_{\rm char}$, increasing as $T_{\rm char}$ increases. At large $T_{\rm char}$, this relation flattens. Only for large $T_{\rm char}$ and long-duration campaigns does the measured delay approach the value expected from the measured centroid of the 1D response function (indicated by the horizontal dashed line). For the BLR model assumed here (Model 2), the number is very close to the lowest points of all three curves.

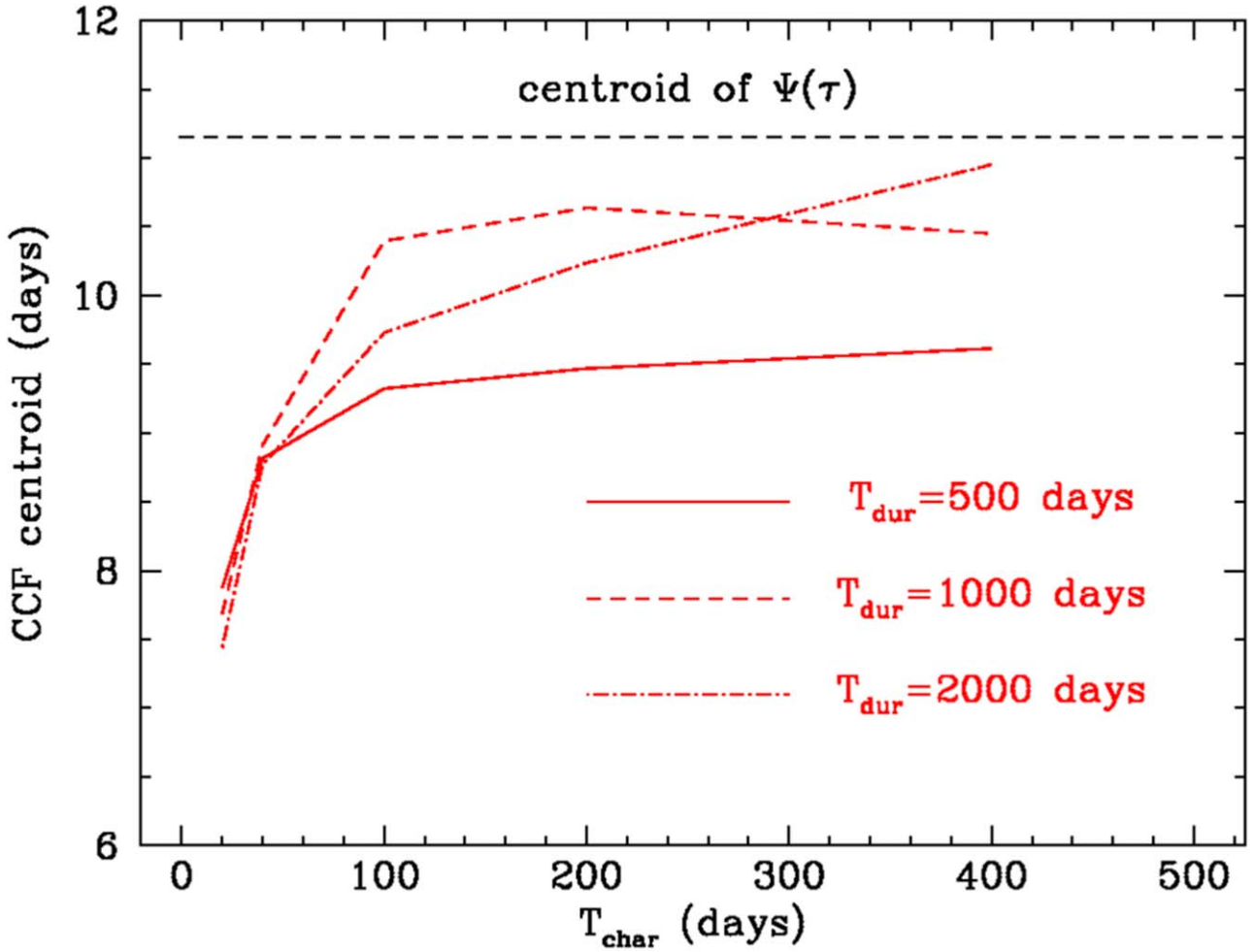

Figure 18. The measured lag (ICCF centroid) for the DC component of Model 2 relative to the driving continuum light curve, here plotted as a function of the characteristic timescale of the driving continuum, for fixed light-curve durations of 500, 1000, and 2000 days, each with 1 day sampling. In all cases, the measured ICCF centroid shows a strong dependence on $T_{\rm char}$, for small $T_{\rm char}$. Only for long light-curve durations does the ICCF centroid approach the MER, and then only for the largest $T_{\rm char}$.

ORCID iDs

Hagai Netzer https://orcid.org/0000-0002-6766-0260
Michael R. Goad https://orcid.org/0000-0002-2908-7360
Aaron J. Barth https://orcid.org/0000-0002-3026-0562
Edward M. Cackett https://orcid.org/0000-0002-8294-9281
Keith Horne https://orcid.org/0000-0003-1728-0304
Erin Kara https://orcid.org/0000-0003-0172-0854
Kirk T. Korista https://orcid.org/0000-0003-0944-1008
Gerard A. Kriss https://orcid.org/0000-0002-2180-8266
Collin Lewin https://orcid.org/0000-0002-8671-1190
John Montano https://orcid.org/0000-0001-5639-5484
Nahum Arav https://orcid.org/0000-0003-2991-4618
Ehud Behar https://orcid.org/0000-0001-9735-4873
Michael S. Brotherton https://orcid.org/0000-0002-1207-0909
Gisella De Rosa https://orcid.org/0000-0003-3242-7052
Elena Dalla Bontà https://orcid.org/0000-0001-9931-8681
Maryam Dehghanian https://orcid.org/0000-0002-0964-7500
Gary J. Ferland https://orcid.org/0000-0003-4503-6333
Carina Fian https://orcid.org/0000-0002-2306-9372
Yasaman Homayouni https://orcid.org/0000-0002-0957-7151
Dragana Ilić https://orcid.org/0000-0002-1134-4015
Shai Kaspi https://orcid.org/0000-0002-9925-534X
Andjelka B. Kovačević https://orcid.org/0000-0001-5139-1978
Luka Č. Popović https://orcid.org/0000-0003-2398-7664
Thaisa Storchi-Bergmann https://orcid.org/0000-0003-1772-0023
Jian-Min Wang https://orcid.org/0000-0001-9449-9268
Fatima Zaidouni https://orcid.org/0000-0003-0931-0868

References

Baldwin, J., Ferland, G., Korista, K., & Verner, D. 1995, ApJ, 455, L119
Baskin, A., & Laor, A. 2018, MNRAS, 474, 1970
Baskin, A., Laor, A., & Stern, J. 2014, MNRAS, 438, 604
Bentz, M. C., Denney, K. D., Grier, C. J., et al. 2013, ApJ, 767, 149
Bentz, M. C., Peterson, B. M., Netzer, H., Pogge, R. W., & Vestergaard, M. 2009, ApJ, 697, 160
Bottorff, M. C., Korista, K. T., & Shlosman, I. 2000, ApJ, 537, 134
Cackett, E. M., Gelbord, J., Barth, A. J., et al. 2023, ApJ, 958, 195
Cackett, E. M., Zoghbi, A., & Ulrich, O. 2022, ApJ, 925, 29
Cai, M., Wan, Z., Cai, Z., Fan, L., & Wang, J. 2024, Univ, 10, 282
De Rosa, G., Peterson, B. M., Ely, J., et al. 2015, ApJ, 806, 128
Dehghanian, M., Arav, N., Kriss, G. A., et al. 2024, ApJ, 972, 141
Dehghanian, M., Ferland, G. J., Kriss, G. A., et al. 2020, ApJ, 898, 141
Du, P., & Wang, J.-M. 2019, ApJ, 886, 42
Fausnaugh, M. M., Denney, K. D., Barth, A. J., et al. 2016, ApJ, 821, 56
Ferland, G. J., Chatzikos, M., Guzmán, F., et al. 2017, RMxAA, 53, 385
Goad, M. R., & Korista, K. T. 2014, MNRAS, 444, 43

Goad, M. R., & Korista, K. T. 2015, MNRAS, 453, 3662
Goad, M. R., Korista, K. T., De Rosa, G., et al. 2016, ApJ, 824, 11
Goad, M. R., O'Brien, P. T., & Gondhalekar, P. M. 1993, MNRAS, 263, 149
GRAVITY Collaboration, Dexter, J., Shangguan, J., et al. 2020, A&A, 635, A92
Hernández Santisteban, J. V., Edelson, R., Horne, K., et al. 2020, MNRAS, 498, 5399
Homayouni, Y., De Rosa, G., Plesha, R., et al. 2023, ApJ, 948, 85
Homayouni, Y., Kriss, G. A., De Rosa, G., et al. 2024, ApJ, 963, 123
Hönig, S. F. 2014, ApJL, 784, L4
Ilic, D., Rakic, N., & Popovic, L. Č 2023, ApJS, 267, 19
Kara, E., Mehdipour, M., Kriss, G. A., et al. 2021, ApJ, 922, 151
Kaspi, S., & Netzer, H. 1999, ApJ, 524, 71
Kaspi, S., Smith, P. S., Netzer, H., et al. 2000, ApJ, 533, 631
Kelly, B. C., Bechtold, J., & Siemiginowska, A. 2009, ApJ, 698, 895
Korista, K., Baldwin, J., Ferland, G., & Verner, D. 1997, ApJS, 108, 401
Korista, K. T., Alloin, D., Barr, P., et al. 1995, ApJS, 97, 285
Korista, K. T., & Goad, M. R. 2019, MNRAS, 489, 5284
Korista, K. T., & Goad, M. R. 2000, ApJ, 536, 284
Koshida, S., Minezaki, T., Yoshii, Y., et al. 2014, ApJ, 788, 159
Kovacevic, J., Popovic, L. Č, & Kollatschny, W. 2014, AdSpR, 54, 1347
Lawther, D., Goad, M. R., Korista, K. T., Ulrich, O., & Vestergaard, M. 2018, MNRAS, 481, 533
Lewin, C., Kara, E., Barth, A. J., et al. 2024, ApJ, 974, 271
Lira, P., Kaspi, S., Netzer, H., et al. 2018, ApJ, 865, 56
Maoz, D., Netzer, H., Peterson, B. M., et al. 1993, ApJ, 404, 576
Mejía-Restrepo, J. E., Trakhtenbrot, B., Lira, P., Netzer, H., & Capellupo, D. M. 2016, MNRAS, 460, 187
Naddaf, M. H., Martinez-Aldama, M. L., Marziani, P., et al. 2023, A&A, 675, A43
Netzer, H. 2013, The Physics and Evolution of Active Galactic Nuclei (Cambridge: Cambridge Univ. Press)
Netzer, H. 2015, ARA&A, 53, 365
Netzer, H. 2020, MNRAS, 494, 1611
Netzer, H. 2022, MNRAS, 509, 2637
Neustadt, J. M. M., Kochanek, C. S., Montano, J., et al. 2024, ApJ, 961, 219
O'Brien, P. T., Goad, M. R., & Gondhalekar, P. M. 1994, MNRAS, 268, 845
Popović, L. Č., Kovačević-Dojčinović, J., & Marčeta-Mandić, S. 2019, MNRAS, 484, 3180
Partington, E. R., Cackett, E. M., Kara, E., et al. 2023, ApJ, 947, 2
Pei, L., Fausnaugh, M. M., Barth, A. J., et al. 2017, ApJ, 837, 131
Peterson, B. M. 2007, in ASP Conf. Ser. 373, The Central Engine of Active Galactic Nuclei, ed. L. C. Ho & J.-M. Wang (San Francisco, CA: ASP)
Peterson, B. M., De Rosa, G., Kriss, G. A., et al. 2020, HST Proposal, 28, #16196
Rees, M. J., Netzer, H., & Ferland, G. J. 1989, ApJ, 347, 640
Rosborough, S. A., Robinson, A., Almeyda, T., & Noll, M. 2024, ApJ, 965, 35
Shen, Y., Horne, K., Grier, C. J., et al. 2016, ApJ, 818, 30
Slone, O., & Netzer, H. 2012, MNRAS, 426, 656
Stern, J., Behar, E., Laor, A., Baskin, A., & Holczer, T. 2014, MNRAS, 445, 3011
Sun, Y.-H., Wang, J.-X., Chen, X.-Y., & Zheng, Z.-Y. 2014, ApJ, 792, 54
Uttley, P., Cackett, E. M., Fabian, A. C., Kara, E., & Wilkins, D. R. 2014, A&ARv, 22, 72
Vanden Berk, D. E., Wilhite, B. C., Kron, R. G., et al. 2004, ApJ, 601, 692
Wamsteker, W., Rodriguez-Pascual, P., Wills, B. J., et al. 1990, ApJ, 354, 446
Weaver, J. R., & Horne, K. 2022, MNRAS, 512, 899
Wills, B. J., Netzer, H., & Wills, D. 1985, ApJ, 288, 94
Zaidouni, F., Kara, E., Kosec, P., et al. 2024, ApJ, 974, 91